Multi-Temporal InSAR for transport infrastructure monitoring: Recent trends and challenges

Macchiarulo, V.; Milillo, Pietro; Blenkinsopp, Chris E.; Reale, Cormac; Giardina, Giorgia

DOI
10.1680/jbren.21.00039

Publication date
2022

Document Version
Final published version

Published in
Proceedings of the ICE - Bridge Engineering

Cite this article
Macchiarulo V, Milillo P, Blenkinsopp C, Reale C and Giardina G
Multi-temporal InSAR for transport infrastructure monitoring: recent trends and challenges.
Proceedings of the Institution of Civil Engineers – Bridge Engineering,
https://doi.org/10.1680/jbren.21.00039

Research Article
Paper 2100039
Received 01/07/2021;
Accepted 02/09/2021

Bridge Engineering

ice Publishing

Multi-temporal InSAR for transport infrastructure monitoring: recent trends and challenges

Valentina Macchiarulo BSc (Hons), MSc
PhD candidate, Department of Architecture & Civil Engineering, University of Bath, Bath, UK; Department of Geoscience & Engineering, Delft University of Technology, Delft, The Netherlands

Pietro Milillo BSc, MSc, PhD
Assistant Professor, Cullen College of Engineering, Department of Civil and Environmental Engineering, University of Houston, Houston, TX, USA; Microwaves and Radar Institute, German Aerospace Center (DLR), Wessling, Germany

Chris Blenkinsopp MEng (Hons), PhD
Senior Lecturer, Department of Architecture & Civil Engineering, University of Bath, Bath, UK

Cormac Reale BE (Hons), PhD
Lecturer, Department of Architecture & Civil Engineering, University of Bath, Bath, UK

Giorgia Giardina MSc, PhD
Assistant Professor, Department of Geoscience & Engineering, Delft University of Technology, Delft, The Netherlands (corresponding author: g.giardina@tudelft.nl)

Worldwide, transport infrastructure is increasingly vulnerable to aging-induced deterioration and climate-related hazards. Often, inspection and maintenance costs far exceed the available resources, and numerous assets lack any rigorous structural evaluation. Space-borne synthetic aperture radar interferometry (InSAR) is a powerful remote sensing technology that can provide cheaper deformation measurements for bridges and other transport infrastructure with short revisit times, while scaling from the local to the global scale. As recent studies have shown InSAR accuracy to be comparable to that of traditional monitoring instruments, InSAR could offer a cost-effective tool for long-term, near-continuous deformation monitoring, with the possibility of supporting inspection planning and maintenance prioritisation while maximising functionality and increasing the resilience of infrastructure networks. However, despite the high potential of InSAR for structural monitoring, some important limitations need to be considered when applying it in practice. In this paper, the challenges of using InSAR for the purpose of structural monitoring are identified and discussed, with specific focus on bridges and transport networks. Examples are presented to illustrate the current practical limitations of InSAR, and possible solutions and promising research directions are identified. The aim of the paper is to motivate future action in this area and highlight the InSAR advances needed to overcome current challenges.

Keywords: bridges/deformation monitoring/infrastructure assessment/remote sensing/roads & highways/safety

Notation

D_1	deformation parameter for linear phase model
$D_{\max}$	maximum deformation rate
D_p	deformation parameter
N	number of images
P	number of models
$2r$	two-way travel distance between radar and target
t_0	time of first acquisition or reference time
t_1	time of second acquisition
α_p	model used to describe actual deformation rate
Δh	residual topographic error
Δr	line of sight displacement (or measured deformation)
Δr_{actual}	actual displacement of target
Δr_{Asc}	line of sight displacement measured from ascending acquisition geometry
Δr_{Desc}	line of sight displacement measured from descending acquisition geometry
Δr_{East}	displacement in east–west plane
Δr_{Up}	displacement in up–down plane
Δr_{v}	displacement vertical projection
ΔT	satellite interferometric revisit time (or temporal baseline)
Φ	phase
$\Delta\Phi$	phase variation (or interferometric phase)
$\Delta\Phi_{\text{defo}}$	phase variation due to target movement
$\Delta\Phi_{\text{earth}}$, $\Delta\Phi_{\text{topo}}$, $\Delta\Phi_{\text{atm}}$, $\Delta\Phi_{\text{noise}}$	phase variation due to flat earth terrain, topography, atmospheric delay and noise, respectively
$\Delta\Phi_n$, $\Delta\Psi_n$	measured and modelled interferometric phase of nth InSAR image
θ	satellite look angle
λ	wavelength
σ_{disp}	dispersion of measured displacement
σ_T	variance of temporal baseline ΔT
$\sigma^2_{\Delta v}$	standard deviation of velocity
σ_Φ	variance of phase noise
ξ_{PS}	temporal coherence
ϕ	azimuth angle

1. Introduction

Modern transport infrastructure is designed for a service life of 50–100 years (van Breugel, 2017). Over this timeframe, structures naturally degrade and thus experience a progressive reduction in structural performance. Design flaws, construction errors, traffic increases, adverse environmental conditions and both natural and anthropogenic disasters can further accelerate the deterioration processes involved, increasing the probability of catastrophic structural failure. In western countries, a major proportion of current transport infrastructure was built between the 1950s and the 1970s. As a result, thousands of assets have now exceeded their intended design lives. The number of structures requiring urgent rehabilitation increases every year and the prioritisation of maintenance activities is a constant challenge for asset managers (Alexakis *et al.*, 2021; Briggs *et al.*, 2017; Pregnolato, 2019) and a key aspect of infrastructure resilience (Achillopoulou *et al.*, 2020).

Structural health monitoring (SHM) is a widely recognised method for evaluating the performance of structures in their operating environment, estimating their residual life and identifying potential damage precursors to ensure safe functionality over the asset's remaining service life (Chang *et al.*, 2003). Traditionally, SHM systems involve a network of in situ sensors that can provide real-time measurements of structural conditions (Worden and Dulieu-Barton, 2004). Established SHM methods include the use of accelerometers, strain gauges and robotic total stations. However, despite the high reliability of the information gathered by such instruments, due to economical constraints and the difficulty in accessing some locations, only a limited number of infrastructure assets are currently equipped with SHM.

Space-borne synthetic aperture radar interferometry (InSAR) is a remote sensing imagery technology that can provide wide-area, low-cost measurements of surface displacements worldwide (Hanssen, 2001; Moreira *et al.*, 2013; Rosen *et al.*, 2000). InSAR systems can operate day and night, and in every weather condition. Due to the availability of historical archives of past satellite images, InSAR can be used retrospectively to study past deformation phenomena. Recent space-borne SAR missions have generated datasets with up to 1 m spatial resolution and 6 day revisit times (Bonano *et al.*, 2013; Milillo *et al.*, 2015). In several geoscience fields, InSAR is already a well-established monitoring technology and enables the study of geophysical processes in glaciology (Goldstein *et al.*, 1993; Milillo *et al.*, 2019a), landslides (Carnec *et al.*, 1996; García-Davalillo *et al.*, 2014), seismology (Dalla Via *et al.*, 2012; Yun *et al.*, 2015), tectonic motions (Bürgmann *et al.*, 2006) and vulcanology (Milillo *et al.*, 2015; Salzer *et al.*, 2017).

Since the late 1990s, advanced signal processing algorithms have been used to analyse long temporal series of InSAR images, enabling surface deformations over time to be reconstructed (Ferretti *et al.*, 2001; Lanari *et al.*, 2004). Multi-temporal (MT) InSAR techniques are based on the identification of targets showing stable scattering behaviour within a series of radar images (Ferretti *et al.*, 2000, 2001). These stable radar reflectors, called permanent scatterers (PSs), are usually associated with architectural elements, exposed rocks or metallic structures, making these techniques extremely effective in urban areas. Furthermore, MT-InSAR is capable of millimetre-scale deformation measurements (Ferretti *et al.*, 2007), reaching an accuracy comparable to ground-based monitoring instruments.

Over the past 20 years, a wealth of literature has demonstrated the capability of MT-InSAR to detect deformations of buildings (Bianchini *et al.*, 2015; Cavalagli *et al.*, 2019; Cerchiello *et al.*, 2017; Chen *et al.*, 2021; Cigna *et al.*, 2014a; Drougkas *et al.*, 2020; Milillo *et al.*, 2018; Peduto *et al.*, 2017; Reale *et al.*, 2019; Shimoni *et al.*, 2017; Zhu *et al.*, 2018), bridges (DePrekel *et al.*, 2018; Milillo *et al.*, 2019b; Selvakumaran *et al.*, 2020), roadways (Infante *et al.*, 2019; Macchiarulo *et al.*, 2021a), railways (Chang *et al.*, 2016) and dams (Di Martire *et al.*, 2014; Milillo *et al.*, 2016a, 2016b), highlighting the potential for this technology to provide measurements of assets that are not included in current monitoring schemes or are difficult to access for visual inspections and conventional SHM systems. With significant data availability and short revisit times, MT-InSAR is ideally suited to provide the inputs to improve damage assessment procedures (Giardina *et al.*, 2019; Macchiarulo *et al.*, 2021b) and decision support models to enable predictive maintenance planning of infrastructure systems (Hadjidemetriou *et al.*, 2021), with the potential to enhance asset longevity and resiliency. MT-InSAR data could be used to develop early warning systems for the identification of potentially damaging structural deformations. If warning of an anomalous structural condition is given in advance, there is time to assess whether the observed deformations are concerning (possibly by taking additional survey measurements), undertake maintenance and, for example, divert traffic around a potentially dangerous structure, thus improving overall network resilience.

However, despite the high potential of this technology for SHM, several challenges arise when applying it in practice, thus limiting the operational use of MT-InSAR. These challenges include

- the availability and distribution of monitoring points for a specific structure
- decomposition of the deformation measurements with respect to the structure's reference system
- the magnitude and rate of maximum detectable movements
- the separation of noise from anomalous structural behaviours

- the assessment of measurement quality
- the accessibility of this technology to the civil engineering community.

The aim of this paper is to discuss the challenges currently limiting the practical use of MT-InSAR technology for transport infrastructure monitoring, to propose solutions for some of the identified issues and to highlight future research directions. Section 2 introduces InSAR, reviews the fundamentals of space-borne SAR sensors, and provides an overview of the technical aspects of the methodology, with a particular focus on MT-InSAR techniques (Section 2.1). Section 3 identifies and discusses the main challenges that need to be overcome for MT-InSAR to be adopted for mainstream structural monitoring usage. Applications to bridges and transport networks are discussed. Each challenge is addressed separately in a different subsection using the following structure: (*a*) the issue is firstly identified from the MT-InSAR perspective and technical limitations are defined; (*b*) the identified problem is analysed with a specific focus on the monitoring of bridges and transport networks; (*c*) possible solutions are suggested and promising research directions are highlighted. Finally, Section 4 summarises the findings and provides closing remarks.

2. Space-borne SAR sensors and InSAR: a theoretical background

Space-borne SAR is an active sensor that can extensively map areas around the globe by transmitting microwave pulses towards the Earth's surface and recording the backscattered returns. The sensor resolution depends on the wavelength and bandwidth of the transmitted signal. For a given acquisition mode, shorter wavelengths provide higher spatial resolutions. Current space-borne SAR sensors operate in three different wavelength bands: L-band (∼24 cm), C-band (∼5.6 cm) and X-band (∼3.1 cm). In SAR images, each pixel is characterised by a certain value of amplitude and phase. The amplitude quantifies the amount of backscattered energy detected by the sensor, and depends on the size, shape, roughness, orientation and dielectric properties of the targets located within the equivalent resolution cell. The phase refers to the signal propagation distance between the sensor and the resolution cell; it is expressed as an angle in the range of 0 to 2π.

SAR satellites move along near-polar orbits and, depending on the satellite's flight direction, they can observe the Earth's surface from south to north (ascending pass) or north to south (descending pass). Space-borne SAR systems have a side-looking imaging geometry, meaning that the sensor is looking sideways with respect to the flight direction (Figure 1). The satellite viewing direction is defined as the line of sight (LoS), and has an inclination (θ) of 20–50° relative to the vertical, or nadir. Depending on the SAR acquisition mode, the swath width can vary from 30 km to 500 km (Moreira *et al.*, 2013). The satellite position over the same area at two distinct times is never identical, and the spatial distance between two acquisition spots is defined as the interferometric baseline. The projection of the interferometric baseline along the direction perpendicular to the satellite LoS is the perpendicular baseline.

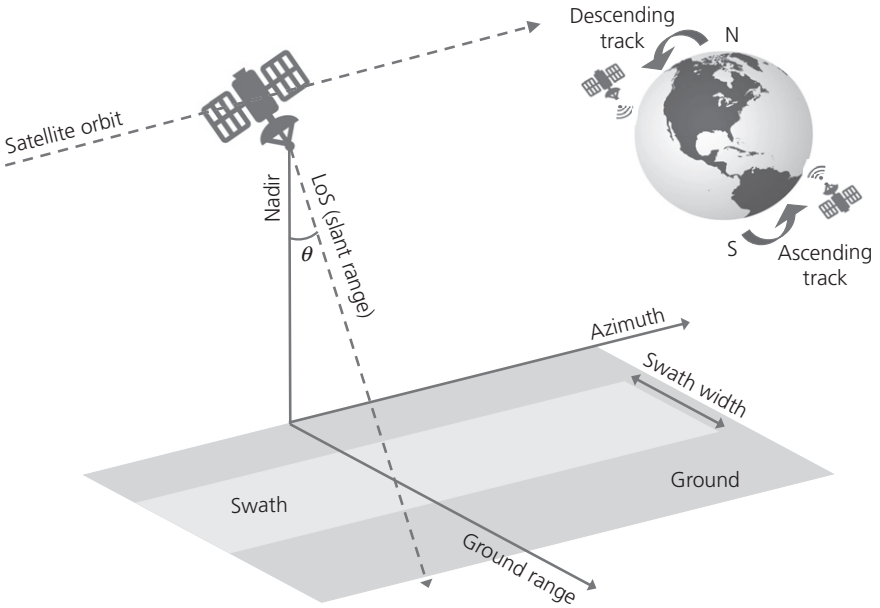

Figure 1. Schematic view of the side-looking acquisition geometry of SAR satellites showing line of sight (LoS) , swath and ascending and descending orbits

Finally, the interferometric revisit time of a satellite determines the minimum time interval (or temporal baseline) required to overpass the same area for generating an interferogram. Currently, SAR satellites have a temporal baseline of 1 day (e.g. the COSMO-SkyMed constellation when multiple satellites in the constellation are used), 3 days (e.g. TerraSAR-X and PAZ) or 6 days (e.g. Sentinel-1A/B).

Since the early 1990s, multiple SAR satellites have been orbiting the Earth, providing observation data with different frequencies and resolutions. Figure 2 provides an overview of past, present and upcoming satellite SAR missions and, for each sensor, the minimum revisit time and spatial resolution are specified. Some of these satellites are no longer operative, such as ERS and Envisat, but have provided valuable archives of data that are still used for studying past deformation phenomena. Active SAR missions include COSMO-SkyMed, TerraSAR-X, RADARSAT-2, Sentinel-1 and ALOS-2. This second generation of space-borne SAR sensors are capable of metre-scale spatial resolutions and revisit times of the order of a few days, providing near-real-time monitoring capability (Bonano *et al.*, 2013; Milillo *et al.*, 2015). Finally, recently launched satellites, such as ICEYE and Capella (Ignatenko *et al.*, 2021; Stringham *et al.*, 2019), or upcoming missions, like HRWS (Gebert *et al.*, 2006), will soon be able to provide data with sub-metre spatial resolution and hourly frequency, with the potential to reach real-time monitoring capability.

InSAR exploits the phase information of a pair of SAR images separated in time to detect changes within the observed area (Gabriel *et al.*, 1989; Massonnet and Feigl, 1998). In InSAR techniques, an interferogram is generated by cross-multiplying two SAR images of the same area on a pixel-by-pixel basis. The phase Φ is proportional to the two-way travel distance between the radar and the target ($2r$) and the wavelength (λ) of the signal:

$$1. \quad \Phi = \frac{2\pi}{\lambda} 2r = \frac{4\pi}{\lambda} r$$

A variation in the phase indicates possible target movements between the two acquisitions (Hanssen, 2001). The phase variation ($\Delta\Phi$) can be written as:

$$2. \quad \Delta\Phi = \frac{4\pi}{\lambda} \Delta r$$

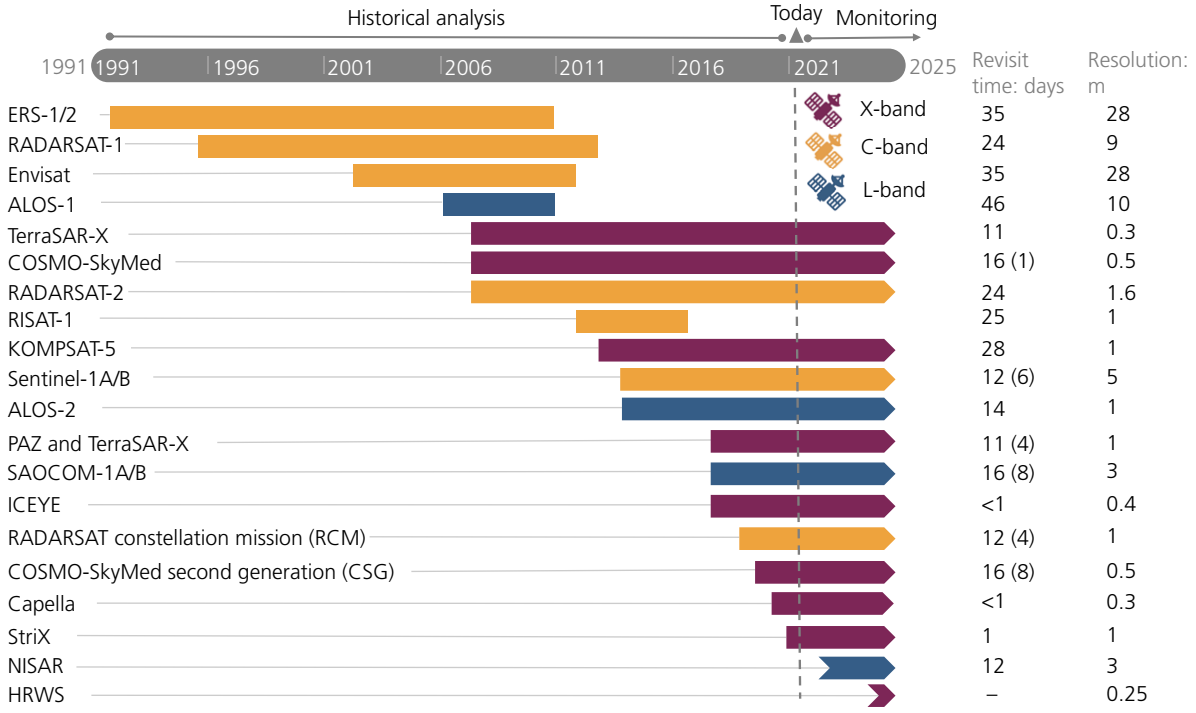

Figure 2. Timeline of past, present and future SAR missions between 1991 and 2025 and their main features (ESA, 2021; Flores-Anderson *et al.*, 2019). Symbols are coloured according to the wavelength band of the sensor. The resolution corresponds to the maximum spatial resolution that the sensor can achieve. For the revisit time, the numbers in brackets indicate the minimum revisit time achievable with the constellation. A full-colour version of this figure can be found on the ICE Virtual Library (www.icevirtuallibrary.com)

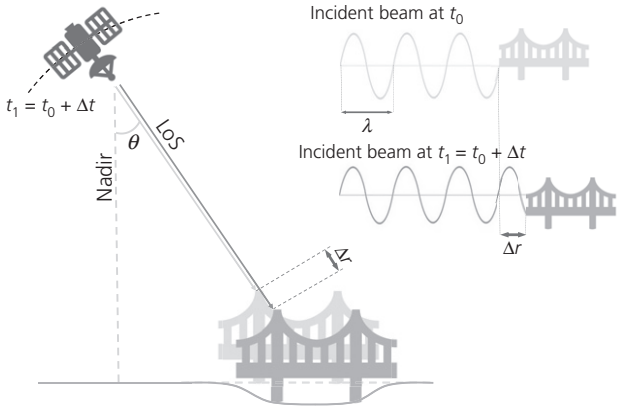

Figure 3. Simplified sketch showing InSAR monitoring of bridge deformations

where Δr is the change in distance travelled by the signal as a consequence of the target movement (Figure 3). However, the interferometric phase $\Delta\Phi$ not only captures the target movements ($\Delta\Phi_{defo}$), but also captures some additional contributions, such as the flat earth terrain $\Delta\Phi_{earth}$, the topography $\Delta\Phi_{topo}$, the atmospheric delay $\Delta\Phi_{atm}$ and some noise $\Delta\Phi_{noise}$:

$$3. \quad \Delta\Phi = \Delta\Phi_{earth} + \Delta\Phi_{topo} + \Delta\Phi_{defo} + \Delta\Phi_{atm} + \Delta\Phi_{noise}$$

The terms $\Delta\Phi_{earth}$ and $\Delta\Phi_{topo}$ are associated with the observation of a different Earth's curvature and a different local topography between two acquisitions of the same area at two distinct times. This is a consequence of the slightly different position assumed by a satellite with respect to its nominal orbit when it overpasses the same geographic region. The atmospheric phase term $\Delta\Phi_{atm}$ corresponds to a signal delay produced by different atmospheric conditions, mainly associated with water vapour content, at two distinct acquisition times. The term $\Delta\Phi_{noise}$ captures possible noise caused by spatial and temporal decorrelations of the radar signal, co-registration errors, orbital errors, soil moisture and residual errors associated with incorrect compensation of the other phase terms. To determine the target displacement, the additional phase terms in Equation 3 need to be estimated and removed. While $\Delta\Phi_{earth}$ and $\Delta\Phi_{topo}$ can be removed by using orbital data and a digital elevation model (DEM) of the area of interest, when only one interferogram is used it is difficult to quantify the atmospheric delay and possible decorrelations of the radar signal. While some methods can be used to mitigate tropospheric (Jolivet *et al.*, 2011) and ionospheric (Gomba *et al.*, 2015) components within single-interferogram approaches, they have been limitedly applied to geophysical phenomena, with rare applications to infrastructure monitoring. In contrast, multi-interferogram methods (i.e. Multi Temporal (MT)-InSAR techniques) enable all the unwanted contributions in Equation 3 to be estimated. The capability of MT-InSAR to reach sub-centimetre accuracy depends on the quality of the data and the joint use of processing parameters and methodologies. The phase of each InSAR image pixel is accurate to a fraction of the radar wavelength (Equation 2), which is of the order of centimetres. Thus, MT-InSAR techniques can theoretically achieve millimetre-scale accuracy on a single deformation measurement.

2.1 MT-InSAR

MT-InSAR is a collection of powerful signal processing techniques that can be used to analyse multiple InSAR images of the same area acquired at different times to measure the displacement over time of point-like targets (Ferretti *et al.*, 2000, 2001). In contrast to other InSAR approaches, MT-InSAR only processes a subset of image pixels, thus resolving the limitations of previous InSAR methods, such as geometrical and temporal decorrelation and atmospheric inhomogeneities. The pixels selected have very distinctive backscattering characteristics. These pixels correspond to highly reflective targets with a stable backscattering over time to the radar and, for this reason are known as Permanent Scatterers (PSs).

During MT-InSAR analysis, PSs are geolocated in three-dimensional (3D) space and their coordinates and elevation can be determined with metre precision. If a sufficient number of PSs are identified across a series of InSAR images, these points can be used to reconstruct a highly accurate approximation of the actual displacement field. PSs form a 'natural geodetic network' (Perissin, 2008), conceptually similar to a network of GNSS (Global Navigation Satellite Systems) stations. This results in a much denser source of measurements than conventional geodetic methods, without any need for installation or maintenance of instrumentation. Field experiments have verified the accuracy of MT-InSAR measurements, confirming the capability of MT-InSAR to reach millimetre-scale accuracy (Ferretti *et al.*, 2007; Rucci *et al.*, 2012). The outcomes of MT-InSAR analysis usually consist of a geospatial dataset containing the PSs identified during the processing and, for each point, the geographic coordinates, elevation, displacement time-series and average velocity are provided. Each point also comes with an index of quality defined as the temporal coherence. All deformation measurements obtained through MT-InSAR analysis are relative to a reference point selected during processing. This reference point is usually selected in a location of known high coherence that is relatively stable in terms of displacement. Since any displacement of the reference point will subsequently affect the displacement measurements of the other PSs, measurements should always be interpreted relative to each other.

Due to their geometric configurations and dielectric properties (Perissin and Ferretti, 2007), bridges, buildings, monuments, metallic objects and exposed rocks are ideal targets for MT-InSAR analysis. Targets that are subjected to significant change (e.g. vegetation) or provide weak reflections (e.g. water basins) do not generate PSs. In urban areas, there can be thousands to tens of thousands of PSs available per square kilometre (Milillo *et al.*, 2018; Perissin and Rocca, 2006), while in extra-urban areas, PSs can still be abundant for viaducts, roadways and railways. These targets are characterised by a very strong reflection and their signal prevails over weaker scatterers that may be present within the same pixel, such as vegetation or water.

Each SAR satellite always overpasses the same area at the same local coordinated universal time (or UTC). Consequently, multiple InSAR images of the same area acquired on different days can capture the seasonal variation of local environmental parameters without being affected by daily temperature and humidity gradients. Thus, thermal expansion effects can be modelled and estimated during MT-InSAR analysis (Fornaro *et al.*, 2013; Gernhardt *et al.*, 2010; Monserrat *et al.*, 2011).

For the specific case of transport infrastructure, the suitability of MT-InSAR for monitoring deformations of bridges, roadways and railways has been investigated in several studies. Some researchers have used historical InSAR images to evaluate retroactively the structural condition of collapsed bridges, showing the potential of this technology for detecting precursor signs of structural failures (Milillo *et al.*, 2019b; Selvakumaran *et al.*, 2018; Sousa and Bastos, 2013). Others have used MT-InSAR to reconstruct the thermal expansion of reinforced concrete or metallic arch bridges (Huang *et al.*, 2018; Lazecky *et al.*, 2016; Qin *et al.*, 2018; Zhao *et al.*, 2017) and compared MT-InSAR deformations with 3D finite-element models of bridge thermal behaviours (Cusson *et al.*, 2018, 2020). Finally, in a few recent studies, MT-InSAR data have been used in combination with in situ sensors, showing the potential of this technology for complementing traditional in situ instruments (Alani *et al.*, 2020; Hoppe *et al.*, 2019; Selvakumaran *et al.*, 2020).

3. Challenges to be resolved and future directions

While recent studies have highlighted the potential of MT-InSAR for monitoring infrastructure assets, several limitations still need to be overcome in order to implement MT-InSAR on an operational basis. In this section, the major challenges facing MT-InSAR as a structural monitoring tool are discussed and possible solutions and promising research directions are highlighted.

3.1 PS availability

In contrast to ground-based monitoring instruments that yield deformation measurements at strategic points on a structure, MT-InSAR is an 'opportunistic deformation measurement method' (Crosetto *et al.*, 2016; Hanssen, 2005) where the PS location is not known before performing the MT-InSAR analysis. Instead, the availability of PSs within an imaged area depends on several factors, as follows.

The number of PSs is limited because they can only be identified in targets that show stable reflective properties over time. Due to their physical nature, bridges, railways and roadways usually satisfy this condition and can generate a high number of PSs. However, in some circumstances, the ability of infrastructure assets to provide stable backscattering over time can be compromised, leading to either a complete or partial loss of PSs. An example is a structure that is covered by snow for some parts of the year. In such scenarios, few – if any – PSs may be available, thereby limiting the monitoring capabilities of MT-InSAR technology. If flooding or snow coverage only occurs for a limited period of time, images affected by these events can be discarded during processing. However, depending on the duration of these events, this might result in large temporal gaps of deformation evolution, and could limit the potential to study seasonal thermal expansion of assets or may introduce unwrapping errors and phase ambiguities in the displacement time-series (Section 3.5). Another example of limited PSs is for structures undergoing maintenance, such as street re-pavement, construction or demolition works. Due to the absence of repeatable targets, these structures may experience a complete or partial loss of PSs. However, this problem can be overcome by using processing methods that deal with temporary or partially coherent targets, such as the Quasi-PS InSAR technique (Perissin and Wang, 2011). Such techniques extend the capability of conventional MT-InSAR and can be used to estimate the deformation of targets that remain stable over a limited time (i.e. Quasi-PSs), thus increasing the spatial density of monitoring points. In several circumstances, the number of PSs can be limited but, in urban areas, several strong reflectors are naturally available. For these strong reflectors, the main lobe and the secondary lobes of the backscattered radiation can be visible in the radar image, risking compromising the association of a pixel to the corresponding target. Side lobes need to be suppressed during processing (Perissin and Rocca, 2006). Similarly, there is ongoing effort in the field to resolve issues associated with radar interference (Reigber and Ferro-Famil, 2005; Zhou *et al.*, 2007).

Another crucial point is the distribution and dimensions of measurable targets with respect to the sensor spatial resolution. For InSAR images with low resolution, it is likely that multiple targets are contained within the same cell, leading to the identification of a relative low number of PSs. This might

prove critical in monitoring structures with a small spatial footprint (e.g. short bridges) and may prevent the acquisition of the minimum number of monitoring points required for damage assessment procedures (Giardina *et al.*, 2019; Macchiarulo *et al.*, 2021b). Consequently, during the development of a monitoring plan, the radar band needs to be selected carefully, based on the study area under consideration, the extent of the structure and the required accuracy. Due to their shorter wavelength, X-band SAR sensors can achieve a finer spatial resolution (up to 30 cm (Prats-Iraola *et al.*, 2012)) than C-band or L-band satellites. They can thus generate a higher number of PSs for short bridges and can even capture discrete measurements for different parts of the structure. As an example, Figure 4 compares the PS density associated with medium-resolution C-band satellites (Figure 4(a)) and high-resolution X-band satellites (Figure 4(b)) for the same motorway junction in Rome, Italy. Figure 5(b) shows the estimated longitudes and elevations of PSs identified on a motorway viaduct in Genoa, Italy. The PSs were obtained by processing the same dataset used by Milillo *et al.* (2019b), which consisted of 130 COSMO-SkyMed ascending images from 2011 to 2018. Thanks to the high resolution of the COSMO-SkyMed data, the estimated PS elevations (Figure 5(b)) captured the three lanes of the asset (Figure 5(a)). However, as a higher resolution is usually connected to a smaller swath, a larger number of frames is needed to observe the same area when compared with lower resolution satellites (Peduto *et al.*, 2015). If PSs are scarce with high-resolution data, MT-InSAR results could be used to optimally identify which assets should have ground-based monitoring systems installed. An alternative solution would be to install corner reflectors on the structures that did not generate sufficient PSs (Ferretti *et al.*, 2007; Selvakumaran *et al.*, 2020). Corner reflectors are cheaper than in situ monitoring instruments and could be installed in strategic locations on the structure to produce sufficient reflection to be picked up as PSs during processing. However, in the case of damage, alignment errors during installation or layers of dust, the visibility of corner reflectors to a satellite could be compromised (Selvakumaran *et al.*, 2021).

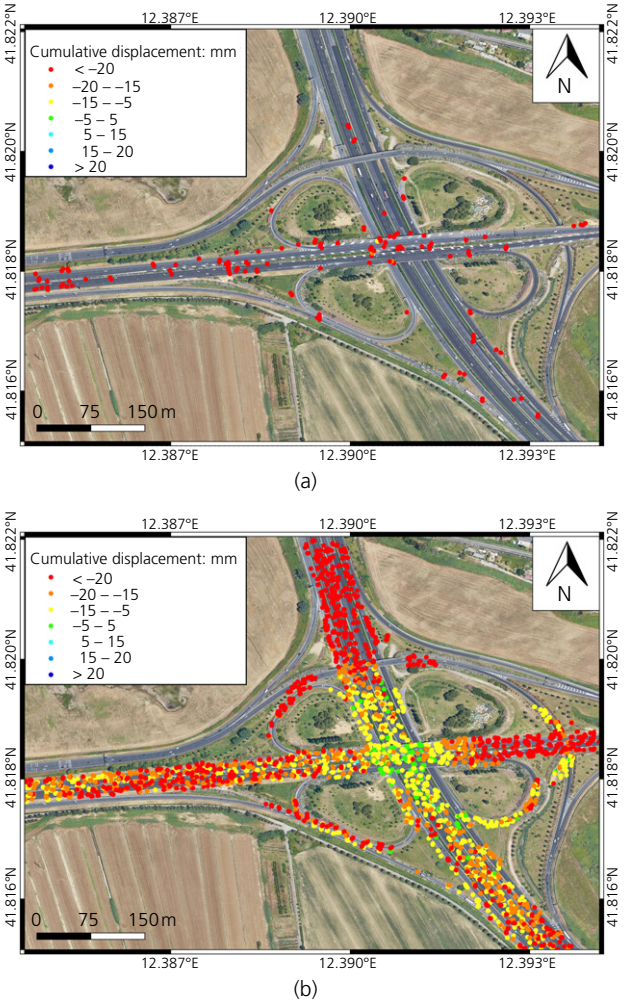

Figure 4. Example of PSs identified over a motorway junction in Rome, Italy, using (a) medium-resolution C-band Envisat data between 2002 and 2010 and (b) high-resolution X-band COSMO-SkyMed data between 2011 and 2014. Each PS is represented by a dot whose colour represents its cumulative displacement along the satellite LoS. Positive and negative values indicate movements towards and away from the satellite, respectively. For both maps, the MT-InSAR datasets described by Costantini *et al.* (2017) were used. A full-colour version of this figure can be found on the ICE Virtual Library (www.icevirtuallibrary.com)

Finally, PSs are usually not evenly distributed – thus, some regions of a structure may be rich in PSs while other regions may have a complete absence of monitoring points. For example, Qin *et al.* (2018) observed a higher number of PSs on bridge piers and a lower amount of PSs on bridge spans, while Hoppe *et al.* (2016) noticed gaps in PSs corresponding to traffic lanes. Reasons for the unequal distribution of PSs include (*a*) the loss of permanent targets due to intense traffic and asphalt radiation bouncing away from the sensor or being absorbed, (*b*) geometrical distortions caused by the oblique viewing geometry of satellites (see Section 3.2) and (*c*) diverse backscattering mechanisms associated with different materials and/or geometrical shapes of different components of the structure (Perissin and Ferretti, 2007). Prior to developing a monitoring plan, a virtual SAR simulator (Auer *et al.*, 2009) with the characteristics of the available sensors can be utilised to evaluate the likely availability and distribution of PSs on a structure. Simulation results could prove useful for (*a*) evaluating the suitability of MT-InSAR technology for monitoring specific structures, (*b*) selecting the best source of data in terms of both the number of and the distribution of monitoring points and (*c*) identifying locations that would require either

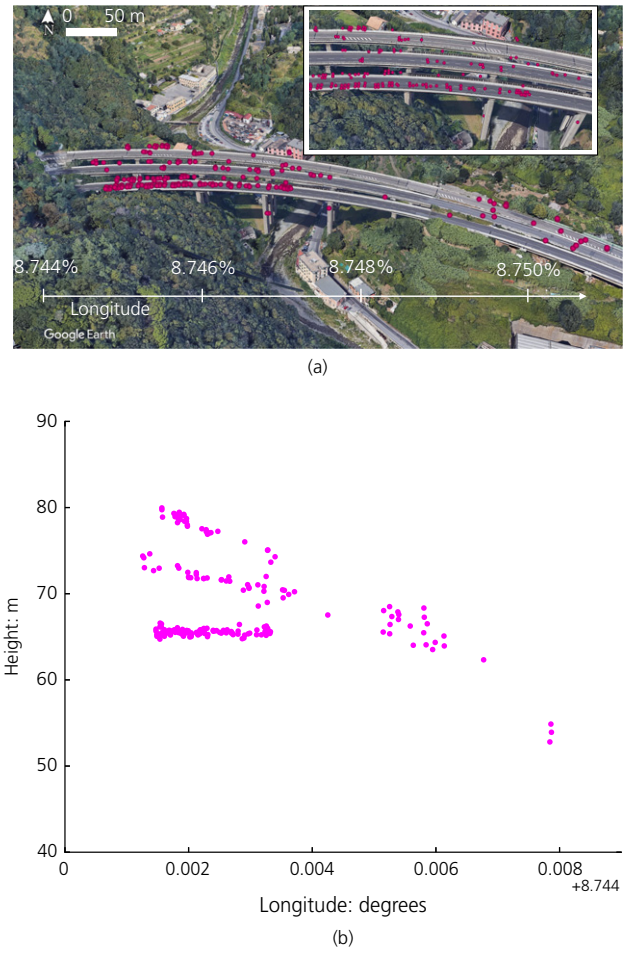

Figure 5. PSs identified on a motorway viaduct in Genoa, Italy: (a) 3D view of PSs on the viaduct from Google Earth; (b) estimated longitudes and elevations of the PSs detected on the asset. Each dot indicates a PS. The PSs were obtained by processing 130 COSMO-SkyMed ascending images from 2011 to 2018 using the software package Sarproz (Perissin *et al.*, 2011). Map data © 2020 Google Earth Pro

corner reflectors or in situ instruments to be installed for adequate monitoring.

3.2 SAR acquisition geometry

As already mentioned, SAR is a side-looking imaging sensor and the 3D space observed by the satellite is then projected into a planar image in radar coordinates (i.e. slant range and azimuth). Consequently, the acquired images can be affected by geometric distortions of the terrain (Hanssen, 2001). Typical distortion effects are shadowing, foreshortening and layover. These effects can be observed when the visibility of the terrain to the radar sensor is compromised as a result of the orientation of the satellite look direction with respect to the local incidence angle.

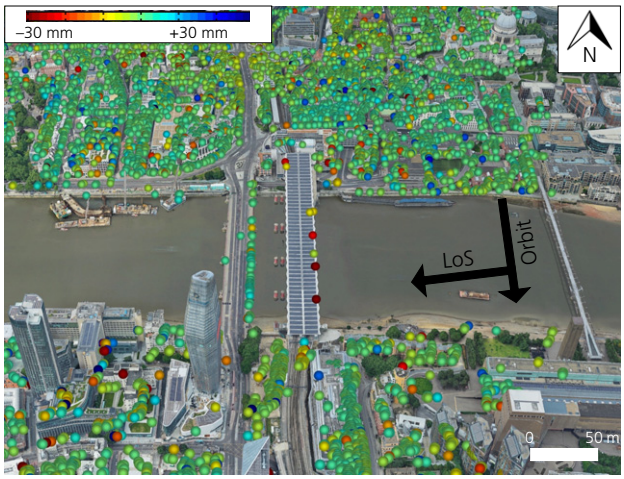

Figure 6. Example of London bridges with the left-hand side mainly in shadow. Each PS is identified by a dot whose colour represents its cumulative displacement along the satellite LOS. The PS deformation time-series are from Milillo *et al.* (2018) and were obtained by processing 72 COSMO-SkyMed descending images from 2011 to 2015. A full-colour version of this figure can be found on the ICE Virtual Library (www.icevirtuallibrary.com)

Shadowing occurs in areas that are hidden from radar illumination. As a consequence, structures located behind very tall buildings or mountain slopes steeper than the satellite look angle will not be visible to the satellite. This also means that PSs can be abundant for structural surfaces facing towards the satellite while the surfaces facing away may be fully or partially obscured. This is shown for two bridges in Figure 6.

Foreshortening can be observed for structures located on moderately steep mountainous slopes facing towards the satellite or for raised structures where the radar signal reaches different parts of the target simultaneously (such as the roof and wall of a building). As a result, the structure is compressed in the image, with the risk that few if any PSs are available.

Layover occurs for bridges located on slopes facing the satellite and with a steepness in excess of the radar look angle, or for very tall buildings. As a consequence, the structure appears tilted in the resulting image, making it difficult to correctly associate PSs.

Finally, since the flight path of satellites is almost parallel to the north–south (N–S) direction, structures with a N–S alignment and characterised by specular reflections may not be visible to the satellite. This is illustrated in Figure 7, where a segment of the E25 motorway in the Liguria region, Italy, is shown in both optical (Figure 7(a)) and radar (Figure 7(b)) images. In Figure 7(b), the edges and guardrails of the motorway mostly appear as bright pixels because they are very reflective. In

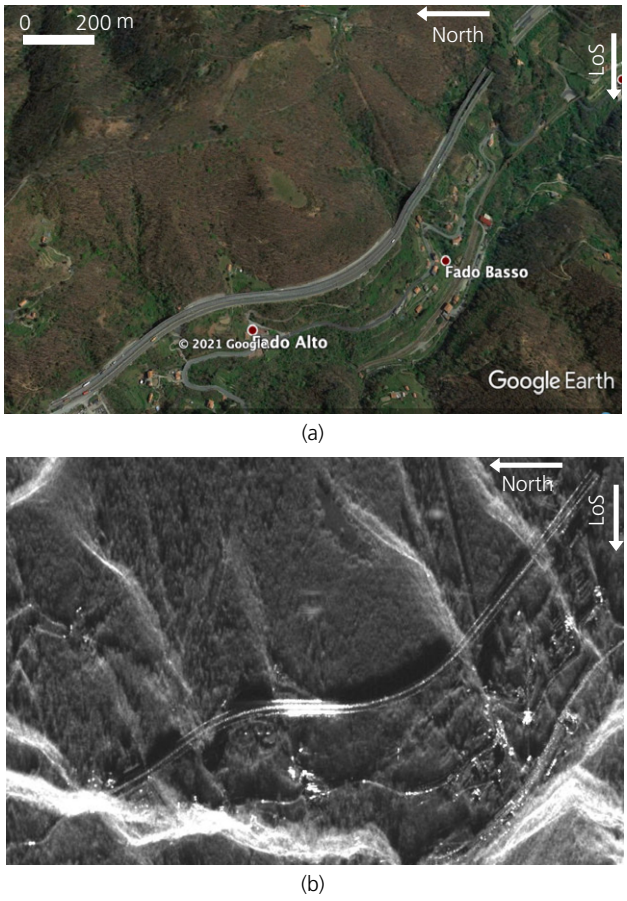

Figure 7. Views of the E25 motorway located in the Liguria region, Italy: (a) Google Earth image; (b) COSMO-SkyMed radar image. In (b), the bright pixels correspond to highly reflective targets, such as the motorway, villages and mountain peaks; the dark pixels correspond to low-reflectivity targets (e.g. vegetation) or to targets in shadow, which appear as black in the image. The COSMO-SkyMed radar image belongs to the InSAR dataset processed by Milillo *et al.* (2019b). Map data © 2021 Google Earth Pro

contrast, the pixels associated with the road pavement tend to generate weaker returns and thus appear darker in the image. Such amplitude information has been recently used for the assessment of road pavement conditions (Meyer *et al.*, 2020). Furthermore, depending on the orientation of the motorway with respect to the satellite's LoS direction, some parts of the infrastructure appear brighter than others and, consequently, may generate more PSs. Figure 7(b) also shows an example of layover: the bright pixels in the lower left-hand corner of the radar image correspond to the mountain peaks located in the top left-hand corner of the optical image (Figure 7(a)).

The use of datasets from both ascending and descending orbits and/or the integration of data from multiple sensors can

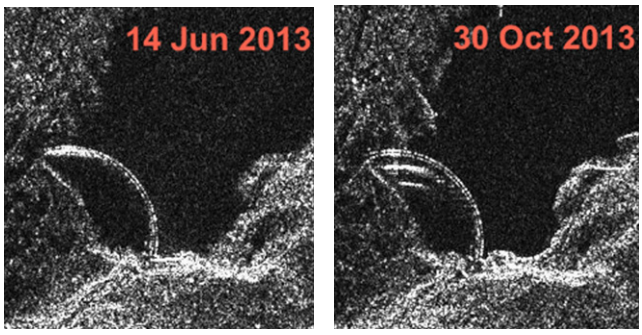

Figure 8. A view of Pertusillo dam, Italy, using COSMO-SkyMed radar images acquired at two different times: (a) single-bounce and (b) double-bounce reflections of the dam crown. The dam crown produced highly intense reflections and thus appears as bright pixels in the radar images; black pixels correspond to water or targets in shadow, such as the basement of the dam. Modified from Milillo *et al.* (2016b) (copyright 2016, with permission from Elsevier)

mitigate these problems. If opposite viewing directions are used, surfaces and targets in shadow in one image may be visible in the opposing direction. Utilising multiple looking directions with different inclinations can improve coverage and sensitivity to displacement on slopes. Prior to the development of a monitoring plan, a simulator taking a high-resolution digital surface model (DSM) and satellite incidence angles as inputs could be used to identify which sensor minimises these effects and consequently predict which locations are likely to be affected by distortions (Cigna *et al.*, 2014b).

Another aspect that can interfere with structural monitoring is double- or multi-bouncing reflections (Balz *et al.*, 2009; Franceschetti *et al.*, 2002). Double-bouncing arises when the radar signal backscattered by the structure interacts with the ground before being reflected back to the radar, while triple-bouncing is when the radar signal undergoes a further reflection back onto the structure. Double- or triple-bouncing echoes can also occur for bridges over water, where the water acts almost like a mirror to the radar, and with superstructures such as arch bridges (Balz *et al.*, 2009; Cusson *et al.*, 2012; Qin *et al.*, 2018). Figure 8 shows an example of the double-bouncing effect observed in radar images of Pertusillo dam, Italy. In contrast to Figure 8(a) where only a single reflection of the dam crown can be observed, the radar image shown in Figure 8(b) recorded multiple reflections of the crown due to a change in the seasonal water level (Milillo *et al.*, 2016b). Furthermore, the basement of the dam is not visible in the images as it is in shadow. Double-bounce and triple-bounce signals are only virtual effects and should be excluded when estimating deformation (Qin *et al.*, 2018).

3.3 Assigning PSs to a structure or part of a structure

Associating PSs with their corresponding structures is another critical aspect of the MT-InSAR technique. The PSs identified during processing usually correspond to different reflecting targets (e.g. bridges, buildings, railways and roadways) located within the area observed by the satellite. To evaluate the performance of a specific structure, the relevant PSs need to be identified and assigned to the target.

During MT-InSAR analysis, PSs are geolocated in 3D space and are thus provided with 3D coordinates (latitude, longitude and elevation). Geospatial tools such as Google Earth or a geographic information system (GIS) can be used to visualise the location of PS data over optical satellite images or base maps, and thus relate deformation to corresponding targets. However, as a consequence of geometric distortions and double-bouncing effects (see Section 3.2), a possible bias in PS geolocalisations, inaccurate height estimations or the presence of multiple targets within the same pixel, PS points can be misassigned and consequently the deformation phenomena misinterpreted.

In several studies, PS data have been analysed in combination with geospatial catalogues of building and infrastructure assets in order to identify points falling within the footprint of structures of interest. While this simple approach usually works well, PSs close to the edges of the structure footprint might not be captured due to the side-looking geometry of SAR sensors or possible localisation errors. This risks losing meaningful information about the behaviour of the structure. Every satellite has a geolocation accuracy that characterises how likely PSs not belonging to a particular structure might be included in the analysis of said structure. Furthermore, due to the possible presence of multiple scatterers within the same pixel, deformation measurements related to targets located within or on a structure, such as traffic lights on roads, could be captured and assigned to the structure. Figure 9 shows an example of geolocation errors observed for PSs extracted on roadways and bridges. Figure 10 shows COSMO-SkyMed MT-InSAR data for a motorway viaduct in the Liguria region, Italy, where some of the PSs assigned to the asset actually correspond to an overhead road sign.

For the analysis of raised structures such as bridges, some researchers have used a filter on PS heights to separate PSs belonging to a structure from PSs located on adjacent ground (Giardina *et al.*, 2019; Huang *et al.*, 2018; Peduto *et al.*, 2017; Qin *et al.*, 2018). For example, Qin *et al.* (2018) interpolated PS heights to extract the points located on a reinforced concrete bridge and discarded all PSs with an elevation more than three standard deviations from the interpolated curve. However, filtering or fitting PS heights is less suitable for analysing assets with a complex shape (e.g. roadway junctions) or linear structures located at the same ground level (e.g. roads and railways). Hoppe *et al.* (2019) and Milillo *et al.* (2019b) used optical images and/or light detection and ranging (LiDAR) data to improve the alignment of PSs on bridges and correctly identify the points belonging to the assets. In several studies, a buffer around the structure's perimeter was defined to isolate the PSs belonging to a given structure from the entire MT-InSAR dataset (Chang and Hanssen, 2015b; Chang *et al.*, 2016; Delgado Blasco *et al.*, 2019; Ge *et al.*, 2009;

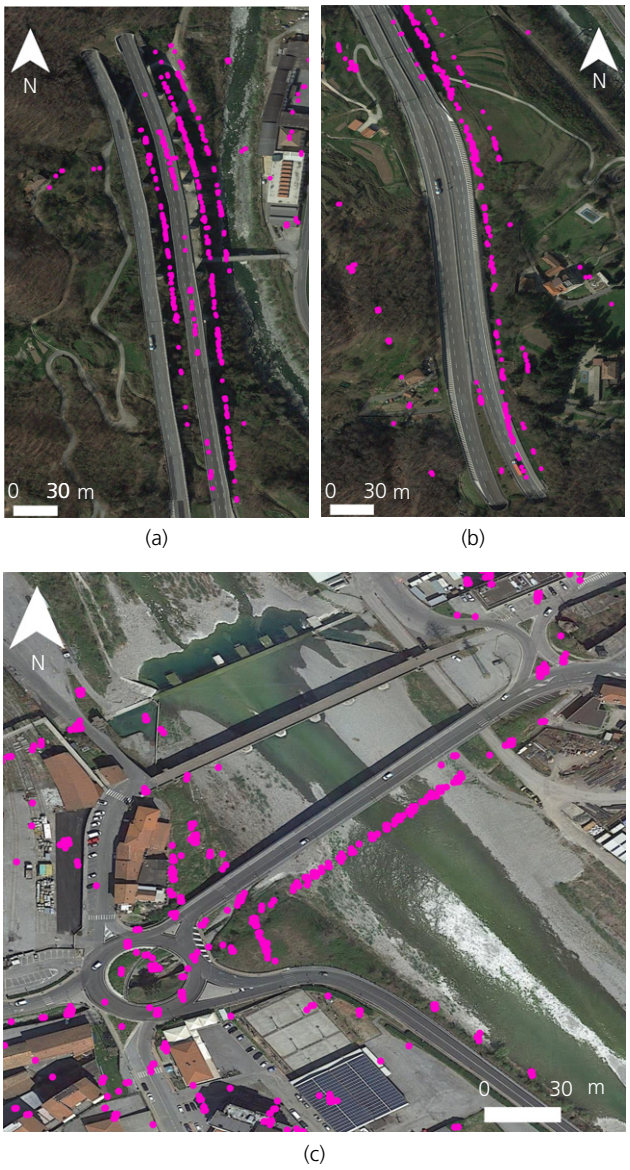

Figure 9. Examples of PS geolocation errors for (a) a motorway viaduct, (b) a motorway segment and (c) a motorway bridge in the Liguria region of Italy. Each dot corresponds to a PS

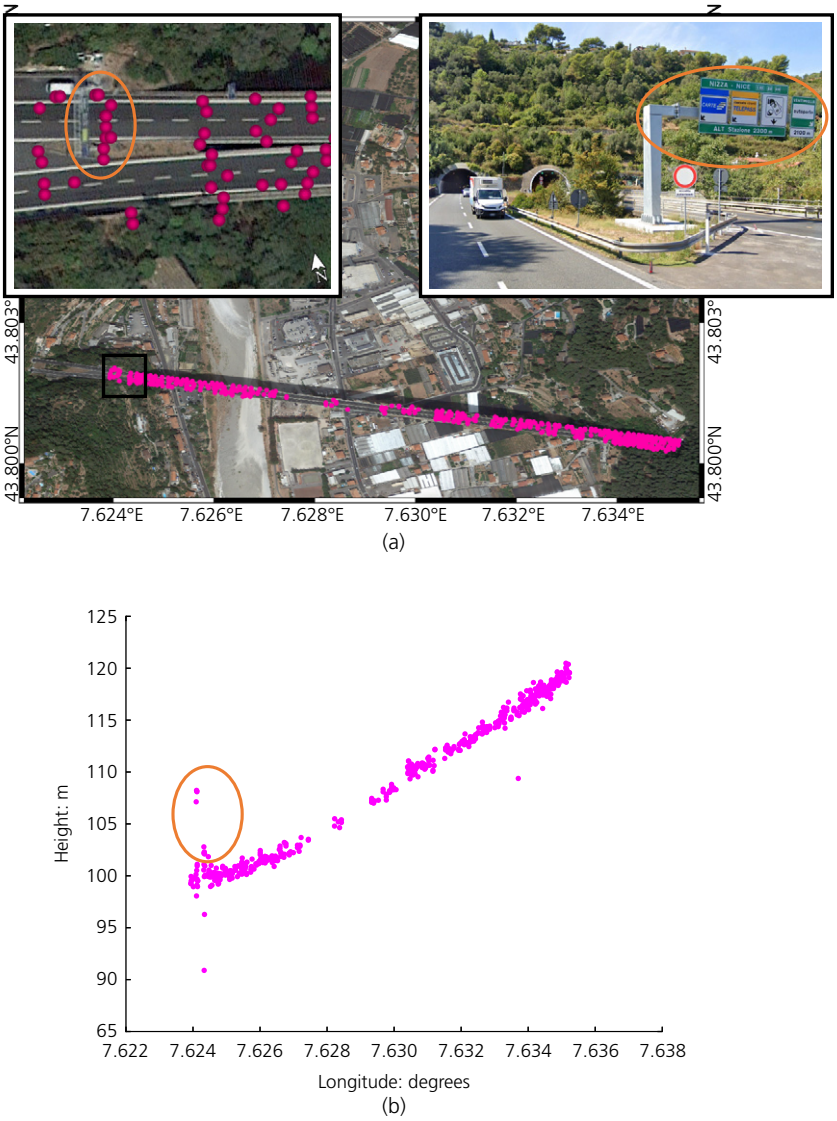

Figure 10. Motorway viaduct in the Liguria region, Italy: (a) PSs superimposed on an optical image of the bridge in Google Earth; (b) estimated longitudes and elevations of the PSs detected on the asset. Each dot corresponds to a PS

Giardina *et al.*, 2019; Infante *et al.*, 2019; Macchiarulo *et al.*, 2021a, 2021b; Peduto *et al.*, 2017). For example, Peduto *et al.* (2017) used a buffer larger than the structure's footprint to compensate for a possible loss of PSs near the edges of the structure. In this case, a PS geolocation precision of 1.5 m was estimated, and PSs located on the building's roof and falling within a 2 m wide buffer around the building perimeter were assigned to the structure. In this specific application, the additional PSs included in the analysis were mostly correct, with only a few invalid PSs (mainly belonging to lamp posts) introduced. Nevertheless, the suitability of this approach needs to be carefully assessed, especially when analysing roadway junctions or bridges located in dense urban areas where PSs from surrounding structures can be easily introduced.

The geolocation accuracy depends on the satellite SAR sensor and the quality of the DEM used during MT-InSAR analysis (Section 2). For satellites with a large orbital tube, such as COSMO-SkyMed, the geolocalisation can be highly accurate, while PS geolocation is much more difficult for satellites with tight orbital tubes like Sentinel (Milillo *et al.*, 2019b). DEMs provide a 3D representation of the terrain and are used during MT-InSAR analysis to estimate and remove the topographic phase ($\Delta\Phi_{topo}$) from Equation 3. However, depending on the

DEM accuracy, the elevation information contained in the DEM can be affected by errors, leading to the risk that $\Delta\Phi_{topo}$ is not properly estimated. The difference between the estimated and the real topographic phase is called the residual topographic error (Δh). This error can affect the rest of the processing, introducing offsets in the PS coordinates, elevations and deformations. To reduce the level of uncertainty in the deformation measurements, geolocation errors need to be minimised. Jung *et al.* (2019) observed that Δh can be estimated as suggested by Perissin and Rocca (2006) or Zhao *et al.* (2017), and then projected onto the east–west and north–west planes to determine latitude and longitude errors:

$$\begin{aligned} \Delta x &= \Delta h \cot\theta \cos\phi \\ \Delta y &= \Delta h \cot\theta \sin\phi \end{aligned} \quad (4)$$

where θ and ϕ are the inclination of the satellite look direction and the azimuth angle, respectively (Figure 1).

DSMs, which provide a 3D representation of the Earth's surface with the inclusion of bridges and other manmade structures, can be used to detect shifts in PS heights (Chang and Hanssen, 2014). In addition to the use of DSMs, PS localisation can be calibrated by installing an artificial reflector at a specific location and measuring its position using GNSS (Nahli *et al.*, 2020; Yang *et al.*, 2016). Finally, to correct residual geolocalisation errors and improve the localisation accuracy of PSs, PS data could be compared with point clouds measured using LiDAR (Chang *et al.*, 2020; Montazeri *et al.*, 2018).

Further errors can manifest when incorrectly associating PSs to specific structural elements. This can be critical when local deformation analyses need to be performed or when interpreting the deformations of structures comprised of multiple construction materials or with a complex shape. While artificial corner reflectors could overcome this problem, their use is not always feasible or practical. Three-dimensional urban models obtained from aerial photos or laser technology could be extremely useful to locate the deformation of assets with a complex shape such as arch bridges or roadway junctions. In a recent study, Selvakumaran *et al.* (2021) showed that PS data analysed in combination with building information modelling (BIM) enabled the visualisation of monitoring data with 3D asset models. To understand which parts of the structure are likely to generate PSs and under what conditions, ray tracing techniques (Auer *et al.*, 2009) can be used in a virtual SAR environment to simulate how different structural shapes and materials influence backscattering.

3.4 LoS deformation measurements

Another crucial aspect affecting InSAR accuracy is that measurements are restricted to a 1D viewing geometry or LoS. This corresponds to the direction connecting the sensor to the target on the ground, and only a projection of the displacements along the LoS direction is reconstructed during MT-InSAR analysis. Apart from rare cases in which the targets move with a velocity parallel to the satellite look direction, a series of InSAR images from a single viewing geometry cannot fully capture the magnitude and direction of the real deformation and, for most cases, the LoS displacements underestimate the real motion (Hu *et al.*, 2014). This concept is illustrated in Figure 11, which shows a target moving along a direction close to the vertical (Figure 11(a)) and a target with a dominant horizontal motion (Figure 11(b)). In Figures 11(a) and 11(b), the target is observed from both ascending and descending acquisition geometries. It can be observed that the magnitude of the measured deformation (Δr) varies according to the satellite acquisition geometry (i.e. ascending

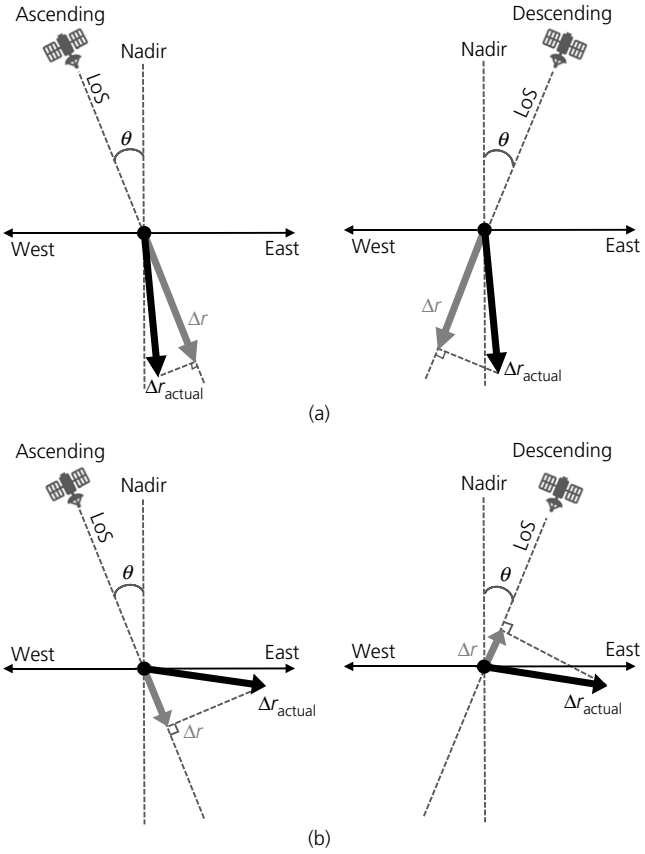

Figure 11. Schematic illustration of the InSAR LoS component of deformation for two targets with movement mainly occurring in (a) vertical direction or (b) horizontal direction. Each target is observed from both ascending and descending acquisition geometries. The black arrow indicates the actual displacement of the target (Δr_{actual}) and the grey arrow corresponds to the displacement measured along the sensor LoS (Δr)

or descending) and the direction of the actual movement (Δr_{actual}). In addition, if the actual motion is mainly horizontal (Figure 11(b)), the two acquisition geometries will measure movements with opposite directions. For example, in Figure 11(b) the displacement measured from an ascending viewing geometry would suggest that the target is moving away from the satellite while, in the descending configuration, movement towards the satellite is detected. Therefore, the level of underestimation increases with the angle between the motion direction and the satellite LoS. For extreme cases where the displacement vector is perpendicular to the LoS direction, the measured displacement is zero, which naturally carries the risk of missing real deformation. Furthermore, since InSAR satellites move along near-polar orbits, this technology is insensitive to N–S movements.

The analysis and interpretation of deformations based on MT-InSAR should be supported by careful consideration of the expected motion, topography and characteristics of the structure under evaluation. Because of the low incidence angle of SAR look directions, MT-InSAR is mostly sensitive to vertical movements. Fuhrmann and Garthwaite (2019) observed that, in some studies, LoS deformations have been interpreted as vertical displacements without discussing the implications of possible horizontal movements (Del Soldato *et al.*, 2016; Solari *et al.*, 2016; Stramondo *et al.*, 2008; Teatini *et al.*, 2005). Prior knowledge of expected motion can be used to make an assumption regarding the direction of the 3D deformation. For example, in areas subjected to uplift, subsidence or tunnelling-induced settlements, motion mainly occurs in the vertical direction and horizontal displacements can be neglected. In these specific scenarios, a common approach is to assume that no horizontal displacements have occurred (Giardina *et al.*, 2019; Milillo *et al.*, 2018; Osmanoğlu *et al.*, 2011; Perissin *et al.*, 2012; Solano-Rojas *et al.*, 2020; Yan *et al.*, 2012) and to estimate the displacement vertical projection (Δr_{v}) by dividing the MT-InSAR LoS measurements by the cosine of the radar incidence angle θ:

$$\Delta r_{\text{v}} = \frac{\Delta r}{\cos\theta} \tag{5}$$

However, if the implications of this assumption are not addressed carefully, depending on the magnitude of the horizontal deformations, the steepness of the local topography and the incidence angle of the satellite looking direction, estimations may result in large errors (Fuhrmann and Garthwaite, 2019). The validity of neglecting the horizontal component should also depend on the structure under analysis. For example, this approximation may be reasonable for studying the tunnelling-induced settlement of stiff buildings (Giardina *et al.*, 2019) or the deformation of roadways in subsiding areas, while bridges are typically subjected to strong thermal effects that may result in large horizontal movements.

To overcome the limitation of 1D LoS measurements, InSAR images from opposite viewing geometries (i.e. ascending or descending) can be used to derive the vertical (up–down) and horizontal (east–west) components of deformation (Milillo *et al.*, 2016b; Wright *et al.*, 2004). This approach involves independent processing of the ascending and descending datasets covering the same location acquired within the same time period to retrieve LoS deformation measurements for each viewing geometry. Then, a co-projection of ascending and descending displacement vectors can be used to resolve the displacement field in the east–west–up–down plane:

$$\Delta r_{\text{East}} = \frac{1}{2}\left(\frac{\Delta r_{\text{Desc}}}{\sin\theta_{\text{Desc}}} - \frac{\Delta r_{\text{Asc}}}{\sin\theta_{\text{Asc}}}\right) \tag{6}$$

$$\Delta r_{\text{Up}} = \frac{1}{2}\left(\frac{\Delta r_{\text{Desc}}}{\cos\theta_{\text{Desc}}} + \frac{\Delta r_{\text{Asc}}}{\cos\theta_{\text{Asc}}}\right) \tag{7}$$

where Δr_{Desc} and Δr_{Asc} are the ascending and descending cumulative displacements, respectively.

Figure 12 shows an example of the decomposition of LoS displacements from ascending and descending acquisition geometry into up–down and east–west components. PS points identified in the ascending and descending datasets are not necessarily the same and might also be affected by geolocation offsets (Gernhardt *et al.*, 2011). Consequently, to integrate datasets from different viewing geometries, pixels in each dataset need to be interpolated in both time and space. However, when this multi-geometry approach is applied to the analysis of bridges, some problems can arise. Satellites with ascending and descending orbits overpass the same area at different times of the day a few days apart from each other. Consequently, due to the different temperatures and/or environmental conditions of the acquired ascending and descending images, bridges can show different thermal behaviours, making reconstruction of the total movement difficult (Hoppe *et al.*, 2016; Selvakumaran *et al.*, 2020). Furthermore, ascending and descending datasets are not always able to provide measurements for a common area. This might be especially prevalent in mountainous regions where geometric distortions (e.g. shadowing, foreshortening and layover) are very likely, or in urban areas where nearby raised structures (e.g. bridges and tall buildings) can lead to a lack of monitoring points (Section 3.2). Finally, for structures characterised by strong deformations along the N–S direction, two viewing geometries are simply not enough to capture N–S displacements. The possibility of estimating the N–S displacement component and

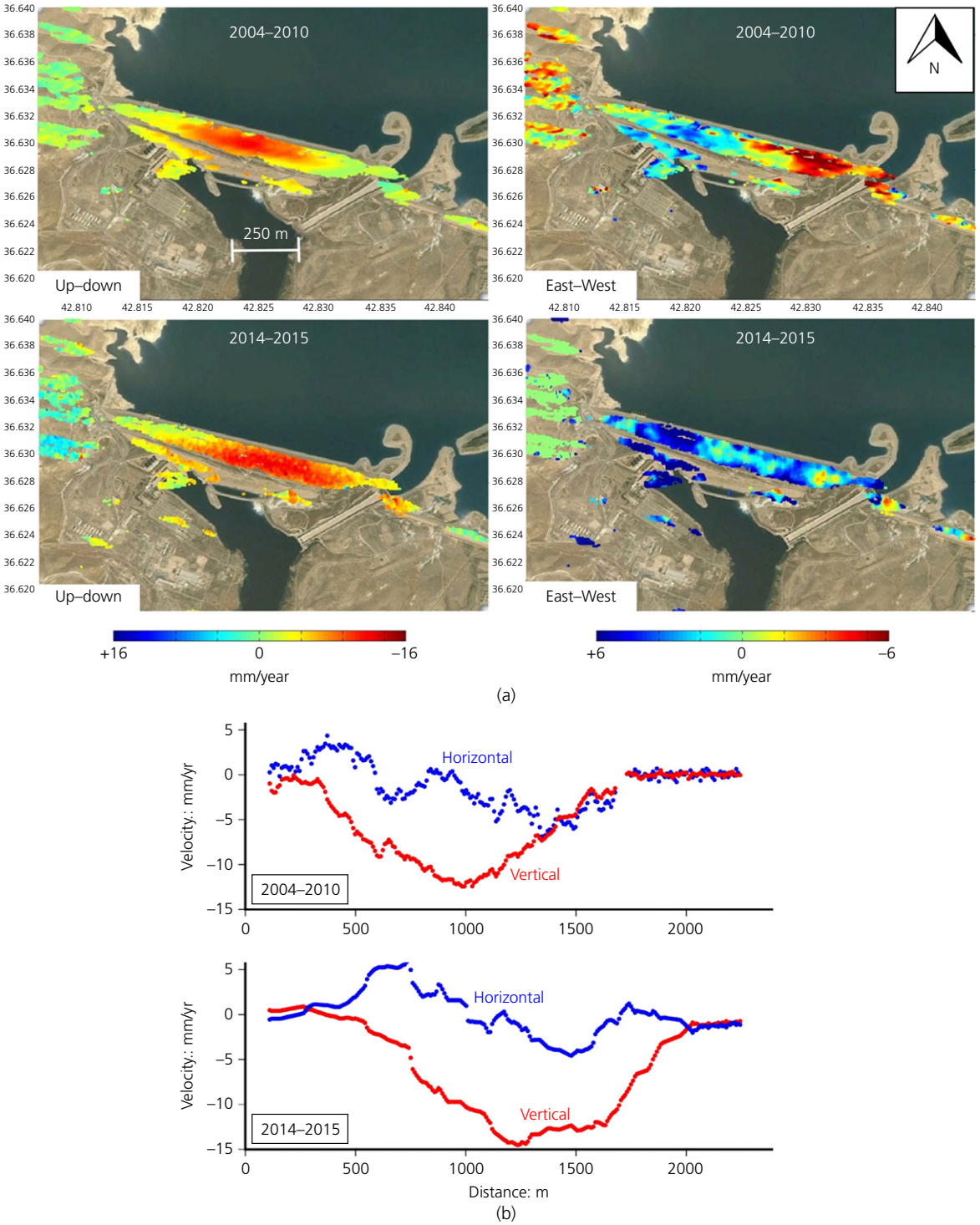

Figure 12. Example of decomposition of LoS velocities into: (a) up–down and east–west displacement rates for the PSs identified on Mosul dam in Iraq; (b) profiles of vertical and horizontal velocities along the longitudinal axis of the dam. The period between 2004 and 2010 was analysed through ascending and descending Envisat images, while from 2014 to 2015 ascending COSMO-SkyMed and descending Sentinel images were used. In (a), negative values correspond to downward and westward movements, respectively. Adapted with permission from Scientific Reports from Milillo *et al.* (2016a) (copyright 2016). A full-colour version of this figure can be found on the ICE Virtual Library (www.icevirtuallibrary.com)

reconstructing a 3D displacement field may be crucial for evaluating the health of bridge structures. However, for bridges orientated along the N–S direction, crucial data are missing.

Some of these problems can be mitigated through the use of multi-geometry/multi-aperture and multi-sensor methods. These methods allow one to combine satellite data acquired from different viewing geometries, frequencies and incidence angles, while simultaneously allowing for the integration of external data sources such as global positioning system or precise levelling (Cuenca *et al.*, 2011a; Fuhrmann *et al.*, 2015; Hu *et al.*, 2014). In contrast to the simple multi-geometry approach – which can only provide deformation measurements in 2D space – a combination of these methods can be used to reconstruct 3D deformations from LoS MT-InSAR measurements. For instance, LoS measurements from different SAR sensors and acquisition geometries can be analysed using the Markov chain–Monte Carlo (MCMC) approach to estimate 3D deformations of analysed assets (Milillo *et al.*, 2016a, 2019b). This approach is useful when an underlying model of the observed deformation is available (Milillo *et al.*, 2016a) or for calculating uncertainties in the 3D displacement field (Milillo *et al.*, 2019b). Furthermore, the use of data from different satellite sensors can increase the range of viewing geometries, potentially providing measurements for structures or regions of structures otherwise in shadow. As an example, Figure 13 shows a schematic illustration of the 3D deformation of key structural elements of Morandi Bridge in Italy. The 3D deformation rates were reconstructed by analysing Sentinel and COSMO-SkyMed MT-InSAR LoS measurements from 2015 to 2018 with the MCMC approach (Milillo *et al.*, 2019b).

3.5 Maximum deformation rates, model approximation and unwrapping errors

The maximum measurable deformation rate depends on the radar wavelength (λ) and the satellite interferometric revisit time (ΔT) (Kampes, 2006; van Leijen, 2014):

$$8. \quad \Delta\Phi_{\text{defo}} = \frac{4\pi}{\lambda}\Delta r = \frac{4\pi}{\lambda}\sum_{p=1}^{P}\alpha_p(\Delta T)\cdot D_p$$

where $\Delta\Phi_{\text{defo}}$ is the deformation phase introduced in Equation 3, α_p corresponds to the model used to describe the actual deformation rate (which is a function of ΔT), D_p is the deformation parameter and P is the number of models adopted.

Due to the periodic nature of the radar phase, MT-InSAR observations are ambiguous in phase; that is, the measurements are wrapped in the interval $-\pi$ to $+\pi$. For two adjacent pixels and two acquisitions separated in time, if the differential deformation phase exceeds $-\pi$ or $+\pi$ the deformation cannot be estimated unambiguously. The problem of resolving such phase ambiguity is called phase unwrapping. Without careful consideration of this technological limitation, large and/or fast structural deformations cannot be detected. MT unwrapping

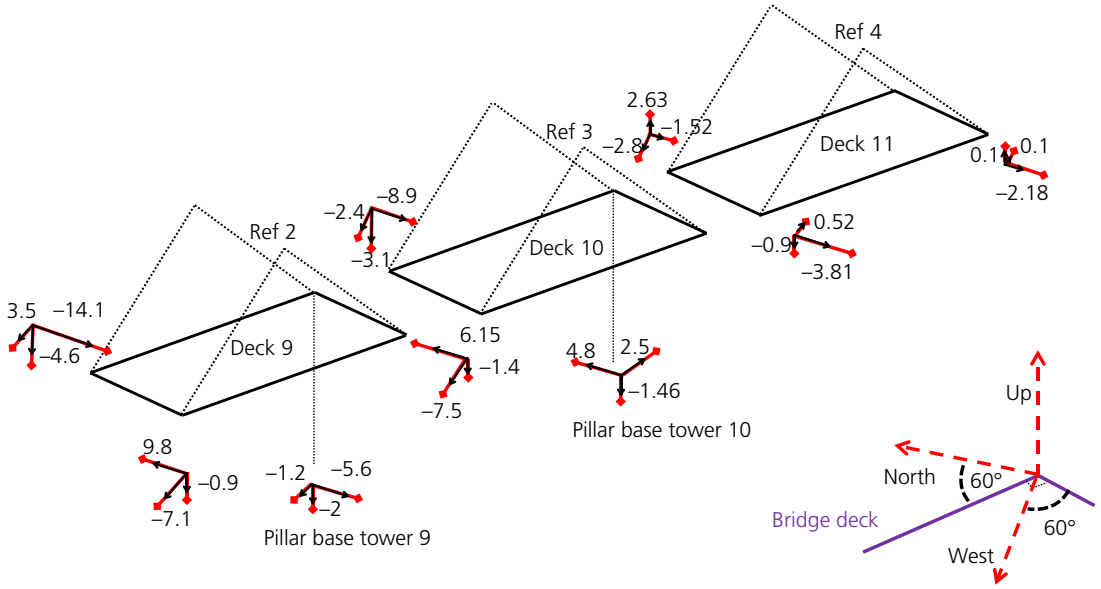

Figure 13. Example of MT-InSAR-derived 3D displacement rates (in mm/year) of the collapsed Morandi Bridge, Italy, from 2015 to 2018. The 3D deformation was reconstructed using the MCMC approach. (Reprinted from Milillo *et al.* (2019b) (copyright 2019) with permission from MDPI)

approaches can be used to resolve such phase ambiguity. However, these methods are usually limited by the assumption of a phase model (Ferretti *et al.*, 2000). For example, for a linear phase model, Equation 8 can be written as:

$$9. \quad \Delta\Phi_{\text{defo}} = \frac{4\pi}{\lambda}\Delta r = \left(\frac{4\pi}{\lambda}\Delta T\right) D_1$$

where D_1 is the average displacement rate observed between the first and last InSAR acquisitions. As the maximum deformation that can, in theory, be estimated over repeat interval ΔT is $\lambda/4$, for a linear deformation model, the maximum deformation rate is (Kampes, 2006; van Leijen, 2014):

$$10. \quad D_{\max} = \frac{\lambda/4}{\Delta T/365.25} \ \text{cm/year}$$

When a linear phase model is used (Equation 9), Crosetto *et al.* (2016) and van Leijen (2014) observed that, for Envisat, TerraSAR-X, Sentinel-1 and ALOS, the maximum deformation rates measurable along the satellite LoS were 14.7 cm/year, 25.7 cm/year, 42.6 cm/year and 46.8 cm/year, respectively. If more complex deformations or higher displacement rates are anticipated, the deformation phase may be modelled through an arbitrary higher order of polynomials, such as quadratic (e.g. $4\pi/\lambda(\Delta T^2 D_2)$) or cubic (e.g. $4\pi/\lambda(\Delta T^3 D_3)$). Table 1 shows the maximum deformation rates that can be measured for selected SAR sensors when a linear, a quadratic or a cubic deformation model is used. It is worth noting that the values shown in Table 1 are only theoretical; in practice, the actual deformation rate also depends on noise in the data and the unwrapping technique used during processing. While longer wavelengths enable larger displacements to be retrieved, they also provide a lower resolution and a higher phase noise.

Some MT-InSAR methods adopt a non-linear deformation model (Bakon *et al.*, 2014; Ferretti *et al.*, 2000). These methods enable the observation of a maximum deformation of $\lambda/2$ over a repeat interval ΔT, enabling higher deformation rates to be estimated. However, depending on the low-pass filter adopted during processing, methods using a non-linear deformation model could incorrectly estimate the atmospheric phase term $\Delta\Phi_{\text{atm}}$, thus leading to an incorrect estimation of deformations. To minimise errors caused by an incorrect estimation of $\Delta\Phi_{\text{atm}}$, there is the need to adopt revisit times as short as possible. Consequently, non-linear methods are more suitable for near-real-time analysis. In this regard, future constellation concepts propose an optimal revisit time of 6 h for atmospheric mitigation during MT-InSAR analysis (Rosen *et al.*, 2019; Zebker and Rosen, 2020). If no prior knowledge exists about the physical model describing the actual deformation field or deformations larger than the theoretical limits are anticipated, such as when assets are located in mining regions (Colesanti *et al.*, 2005), MT-InSAR measurements could be complemented with in situ measurements or integrated with amplitude-based SAR techniques (Casu *et al.*, 2011; Crosetto *et al.*, 2016). For such techniques, the amplitude information of two or multiple SAR images is used to determine the pixel offset at the same positions, providing a 2D estimate of deformation.

Other methods that do not require the assumption of a displacement model during processing are small-baseline techniques (Berardino *et al.*, 2002; Lanari *et al.*, 2004). In these methods, the interferograms in a given series of InSAR images are divided into multiple subsets with small temporal baseline ΔT. Then, the interferograms within each subset are unwrapped in space before time-series analysis is performed. However, Ansari *et al.* (2020) and Usai (2003) observed that small-baseline methods are likely to introduce systematic biases in the deformation phase, risking overestimation of the actual displacement. In the scientific community, discussions on the topic are currently ongoing, thus highlighting the challenging nature of the problem (De Luca *et al.*, 2021; Milillo *et al.*, 2020).

Table 1. Theoretical maximum deformation rates ($D_{\max}$) measurable for selected SAR sensors when a linear ($4\pi/\lambda(\Delta T D_1)$), quadratic ($4\pi/\lambda(\Delta T^2 D_2)$) or cubic ($4\pi/\lambda(\Delta T^3 D_3)$) deformation model is used. It is noted that higher displacement rates can be measured when constellation revisit times are used

		$D_{\max}$: cm/year		
SAR sensor	**ΔT: days**	Linear model	Quadratic model	Cubic model
ALOS-1	46	46.8	186	985.4
Envisat	35	14.7	76.2	530
RADARSAT-1	24	21.3	162	1644
COSMO-SkyMed	16	17.7	202	3073
Sentinel-1	12	42.6	648.5	13159
TerraSAR-X	11	25.7	427	9457.4

Temporal sampling of deformations is limited by the satellite revisit time. Since most current SAR satellites yield data every 6–24 days, MT-InSAR can effectively monitor slow deformation phenomena, evolving over months or years. Consequently, this technology is appropriate for long-term monitoring of aging assets (Macchiarulo *et al.*, 2021a; Milillo *et al.*, 2019b), where it could provide data at a higher frequency than visual inspections. Similarly, it could be used for assessing the impact of residual settlements on existing structures in post-tunnelling scenarios (Giardina *et al.*, 2019; Macchiarulo *et al.*, 2021b). In its current form, MT-InSAR cannot be used for real-time monitoring and is thus not suitable for monitoring infrastructure response during fast-deformation phenomena or catastrophic events such as typhoons, monsoon events and earthquakes. Recent satellite developments suggest that data with a higher temporal resolution could become available relatively soon. Constellations of satellites, like the COSMO-SkyMed constellation or RADARSAT constellation mission, may be used to achieve shorter repeats, while private agencies could be able to reach daily or hourly imaging capabilities by the end of 2021, with the possibility of providing commercial data for MT-InSAR applications in intervals of 4–6 h (Ignatenko *et al.*, 2021; Stringham *et al.*, 2019).

To remove the 2π ambiguity and produce a continuous signal during MT-InSAR analysis, several phase unwrapping techniques have been developed (Costantini *et al.*, 2012; Cuenca *et al.*, 2011b; Hooper and Zebker, 2007; Luo *et al.*, 2019; Wu *et al.*, 2018). These techniques mostly use residual or least-squares methods to unwrap the differential phase in both space and time. However, no universally accepted solutions have been found yet, and unwrapping errors remain a major source of uncertainty in MT-InSAR data. Unwrapping errors are often manually removed during post-processing. If they are not identified and resolved, the dataset will contain anomalies and will not align with other monitoring instruments, increasing the risk of misinterpreting the real deformation response. Unwrapping errors can be recognised when the displacement difference between two subsequent acquisitions is equal to, or close to, half a wavelength. For example, Figure 14 shows two unwrapping errors in the time domain for a PS detected on a Los Angeles highway after processing Sentinel data between 2016 and 2019 (Macchiarulo *et al.*, 2021a).

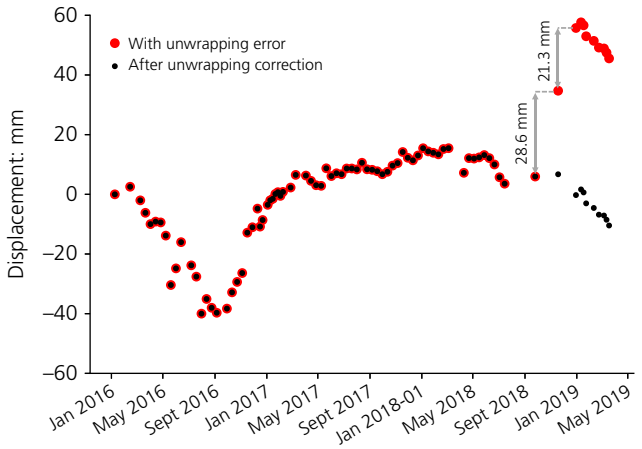

Figure 14. Example of deformation time series for a specific PS with unwrapping errors (red dots) and without unwrapping errors (i.e. after correction) (black dots). To emphasise the difference, a different size is used for the black and red dots. The displacement time-series was obtained from 84 images acquired by Sentinel, which operates at $\lambda = 5.6$ cm

3.6 Coherence

Another possible source of error is the criteria used to estimate the reliability of deformation measurements. The quality of MT-InSAR data is quantified in terms of its temporal coherence ξ_{PS}:

$$11. \quad \xi_{PS} = \left| \frac{1}{N} \sum_{n=1}^{N} e^{i(\Delta\Phi_n - \Delta\Psi_n)} \right|$$

where N is the number of InSAR images used during processing and $\Delta\Phi_n$ and $\Delta\Psi_n$ are the measured and modelled interferometric phase of the nth InSAR image, respectively. The temporal coherence can vary between 0 and 1, and is inversely proportional to the signal-to-noise ratio. Thus, the higher the coherence, the more accurate and reliable subsequent displacement estimates will be, according to the phase model adopted.

To minimise the level of noise in measurements and identify only highly reliable scatterers, PSs are usually selected by applying a coherence threshold. At present, no common agreement exists about the optimal coherence threshold. In some studies, all PSs with a coherence greater than 0.6 or 0.7 are selected (Ma *et al.*, 2019; Milillo *et al.*, 2019b; Selvakumaran *et al.*, 2020) while, in others, more conservative values such as 0.8 or 0.9 are adopted (Cusson *et al.*, 2018; Giardina *et al.*, 2019; Macchiarulo *et al.*, 2021b; Sousa and Bastos, 2013). It is worth noting that high threshold values not only reduce the probability of false alarm rates but also reduce the number of PSs selected (Figure 15); consequently, the risk of losing valuable information increases. If the coherence threshold is too low, noisy points will be introduced into the analysis and the structural deformation could consequently be misinterpreted. Thus, to successfully exploit MT-InSAR technology, an optimal balance between the number of monitoring points and the reliability of estimates needs to be found.

Theoretically, the higher the coherence (ξ_{PS}), the lower the dispersion (σ_{disp}) of the estimated measurements

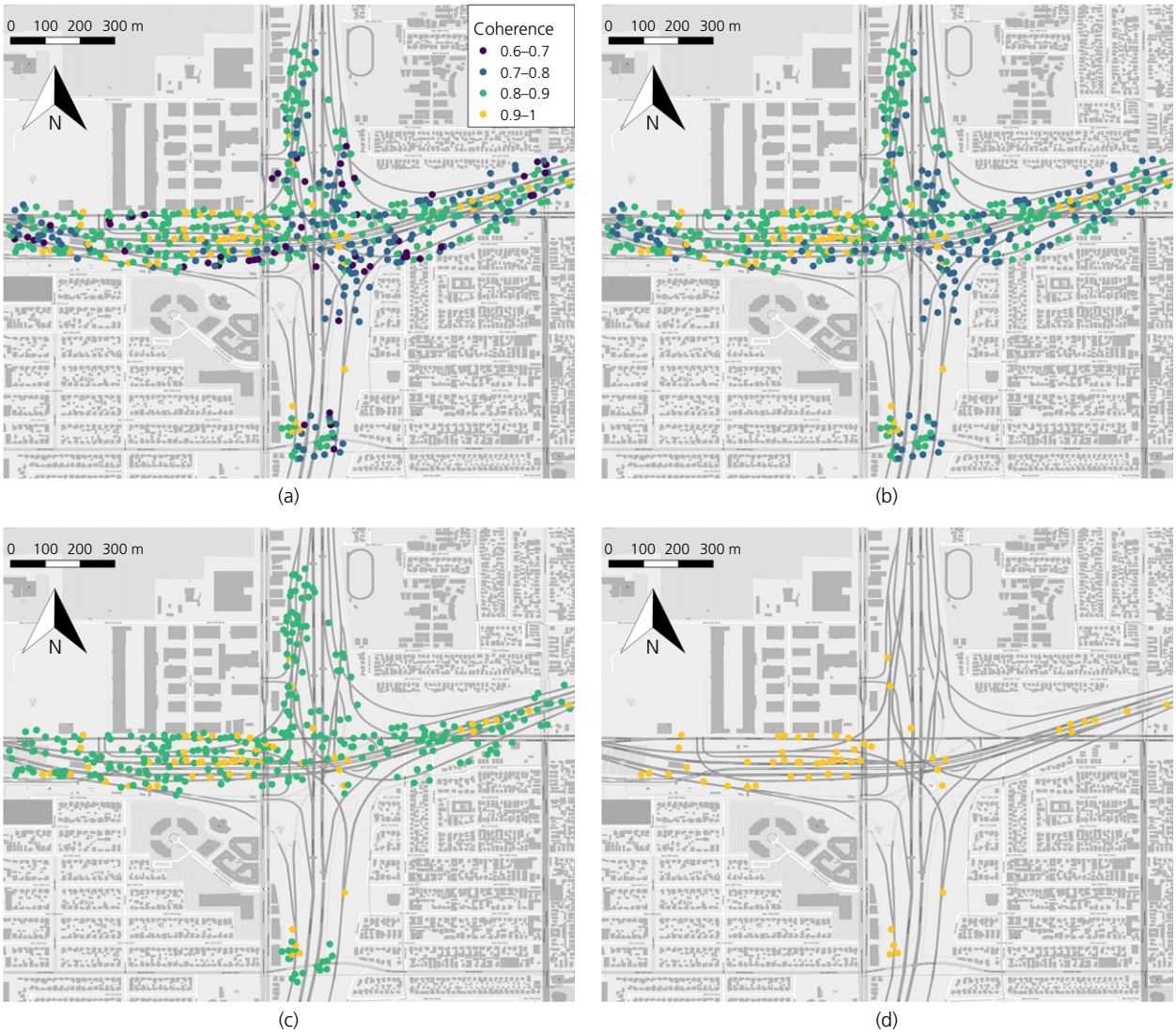

Figure 15. Example of PSs extracted on a highway junction in Los Angeles, USA, using coherence threshold of (a) 0.6, (b) 0.7, (c) 0.8 and (d) 0.9. The PSs were obtained by processing 84 ascending Sentinel images from 2016 to 2019. A full-colour version of this figure can be found on the ICE Virtual Library (www.icevirtuallibrary.com)

(Colesanti *et al.*, 2003):

$$\sigma_{\text{disp}} \approx \frac{\lambda}{4\pi}\sqrt{-2\ln|\xi_{\text{PS}}|} \text{ mm} \quad (12)$$

The number of images used during processing (N) and the wavelength of the satellite SAR sensor (λ) also impact measurement uncertainty. For example, Colesanti *et al.* (2003) observed that for, C-band satellites (e.g. ERS/Envisat and Sentinel), ξ_{PS} values of 0.8, 0.9, 0.95 and 0.975 correspond to σ_{disp} values of 3, 2, 1.44 and 1 mm, respectively. Based on these coherence values, theoretical σ_{disp} values for X-band, C-band and L-band satellites are shown in Table 2. Similarly, the standard deviation of velocity ($\sigma^2_{\Delta v}$) decreases for shorter wavelengths and as N increases. For a linear phase model:

$$\sigma^2_{\Delta v} \approx \left(\frac{\lambda}{4\pi}\right)^2 \frac{\sigma^2_{\Phi}}{N\sigma^2_T} \quad (13)$$

where σ_T is the variance of the temporal baseline ΔT and σ_Φ is the variance of the phase noise, which is a function of the temporal coherence ($\sigma_\Phi \approx (-2\ln|\xi_{\text{PS}}|)^{1/2}$). Equations 12 and

Table 2. Theoretical dispersion values (σ_{disp}) of PS deformation measurements corresponding to PSs with different coherence for X-band, C-band and L-band SAR satellites

Coherence, ξ_{PS}	σ_{disp}: mm		
	X-band (3.1 cm)	C-band (5.6 cm)	L-band (24 cm)
0.8	1.65	3	12.75
0.9	1.13	2	8.77
0.95	0.79	1.44	6.12
0.975	0.56	1	4.3

13 suggest that, depending on the number of images adopted during processing and the wavelength of the satellite SAR sensor, different coherence thresholds could be adopted. According to Perissin and Wang (2011), when the number of images available is small (e.g. $N < 25$), a minimum temporal coherence of 0.9 should be used; while images are more abundant (e.g. $N > 60$), the coherence threshold can be decreased to 0.7. However, such values were proposed on the basis of theoretical modelling (Colesanti *et al.*, 2003) and only apply to C-band SAR satellites with a large orbital tube, such as ERS and Envisat. To the authors' knowledge, no studies show the impact of setting different coherence thresholds for real scenarios and for SAR satellites with different characteristics.

The efficacy of a coherence selection method further depends on the accuracy of the deformation model used during the processing (Colesanti *et al.*, 2003). Most MT-InSAR methods use a linear deformation model. Consequently, in areas characterised by highly non-linear movements, a coherence drop is observed due to the lack of conformity between the actual deformation and the adopted model. In these scenarios, low coherence values may be interpreted as noise in the data and can lead to some PSs being incorrectly classified as unreliable and discarded, or the estimated deformations may underestimate the actual displacement. Naturally, this has significant implications for infrastructure monitoring, where cracking, material deterioration and damage processes are frequently described by non-linear trends (Chang *et al.*, 2003). Some MT-InSAR algorithms enable the use of a non-linear deformation model (Bakon *et al.*, 2014; Ferretti *et al.*, 2000). However, these methods are usually computational demanding and thus unsuitable for regional analysis.

Bridges, buildings and transport infrastructure usually remain highly coherent over a time-series of InSAR images. However, in the presence of snow coverage, traffic (Milillo *et al.*, 2020), maintenance, construction or demolition works (Section 3.1), these targets may lose coherence and behave as Quasi-PSs. In addition to the use of techniques dealing with this specific problem (Perissin and Wang, 2011), a recent study by Refice *et al.* (2020) explored the possibility of using parameters other than coherence to discriminate non-linear deformations or partially coherent targets from a subset of PSs with very low coherence. In that study, fuzzy entropy – a parameter completely independent from the model adopted during processing – was used to characterise InSAR time-series on both simulated and real data. Despite the promising results, the need for a very long series of images ($N > 180$) to achieve stable results may be the limiting factor for this approach and more studies are needed to assess its robustness.

3.7 Processing errors due to user expertise

Specialised processing skills remain a barrier preventing the widespread adoption of MT-InSAR data within the civil engineering industry. Estimating deformations from long temporal series of InSAR images involves a number of non-intuitive steps, which can be challenging for non-specialists. Results of MT-InSAR analysis rely heavily on the assumptions made and the parameters chosen during processing. Chang and Hanssen (2015a) observed that, depending on the employed processing criterion and threshold values used, very different outcomes could be obtained for the same area (Chen *et al.*, 2012; Xie *et al.*, 2010) or for the same dataset (Sousa *et al.*, 2011). Over recent years, several software packages reproducing the core steps of MT-InSAR analysis have been developed. These user-friendly programs are designed for a wide range of different applications and provide highly flexible environments. However, users with insufficient experience could easily adopt false assumptions or inappropriate input parameters without fully understanding their influence, thus compromising the results.

The development of user-ready products can minimise these problems, keeping the use of MT-InSAR data accurate and easy at the same time. Open-source MT-InSAR datasets processed by radar experts are starting to become available (Costantini *et al.*, 2017; Crosetto *et al.*, 2020; Raspini *et al.*, 2018), making MT-InSAR-derived measurements more accessible to stakeholders. To facilitate user-friendliness, data should be provided in a format that is easily accessible through standard GIS platforms and with detailed metadata.

To guide users with no radar experience through the processing, the practical impact of different assumptions and parameters should be investigated. There is therefore a need for more comparative and systematic studies that compare different processing methods and assess the sensitivity of results to input parameter settings and circumstances. This could help to identify the most appropriate approach for specific structural monitoring applications, with the further possibility of standardising the procedure.

Finally, while consolidated knowledge and experience in MT-InSAR technology may be crucial to secure reliable results, deep knowledge of the processes governing structural deformation is fundamental to correct interpretation of MT-InSAR measurements for structural monitoring applications. The next generation of civil engineers should be trained in this remote sensing technique, while collaborations between radar scientists and civil engineers should be encouraged and communication strengthened.

4. Conclusions

MT-InSAR has the potential to be a cost-effective tool for transport infrastructure monitoring, enabling infrastructure managers to move from reactive to proactive maintenance, preserving functionality while increasing network resilience. MT-InSAR can provide highly accurate deformation point measurements over wide areas at fine spatial resolution, enabling the observation of both individual assets and whole networks. These measurements could be used to estimate structural performance indicators or provide the inputs for prediction procedures, with the potential to provide asset managers with the data they need to make risk-related lifecycle decisions (e.g. maintenance scheduling) to maximise asset utility efficiently and increase network resilience. As this technology operates remotely, it is environmentally friendly and safer than ground-based monitoring. It could complement and extend upon in situ monitoring, thus simplifying logistics and reducing costs. Thanks to the availability of historical archives of SAR images, MT-InSAR enables the study of past structural failures and construction incidents for which monitoring data is not available, with the potential to provide new insights into failure mechanisms.

However, despite numerous studies demonstrating the potential of MT-InSAR technology for structural monitoring, several challenges still need to be addressed. In this paper, the major current challenges were analysed from a structural monitoring perspective. The following conclusions were drawn from this work.

- Due to the 'opportunistic' nature of MT-InSAR techniques, the locations and distribution of monitoring points are known only after completion of the MT-InSAR analysis. Consequently, the availability of PSs for a specific structure cannot be guaranteed. In addition, due to, for example, snow coverage and maintenance activities, the pixels related to a structure can lose coherence within the series of InSAR images, causing complete or partial loss of PSs. For structures characterised by a lack of PSs, corner reflectors could be used to reproduce artificial scatterers and 'supply' monitoring points. Ray tracing techniques could be used to create a virtual SAR environment with the characteristics of available SAR sensors. This environment could then be used to predict the capability of the structure to generate PSs based on its material properties and in relation to existing SAR satellites. Finally, Quasi-PS InSAR techniques could be used to deal with partially coherent targets.
- Radar images provide 2D representations of the real world. For raised structures, steep topography or in urban areas, some geometric distortions can be observed. In addition, scattering interactions between a structure and nearby surfaces can be recorded in InSAR images, producing geometrical artefacts. The use of MT-InSAR data from multiple satellites and acquisition geometries can improve the chance of observing structures in shadow, while simulations can be used to predict geometrical distortions and artefacts before undertaking processing.
- Correctly associating monitoring points to the corresponding structure or to a specific part of that structure can be complicated by the aforementioned artefacts and distortions, possible geolocation offsets, the presence of additional targets on the structure (e.g. traffic lights and road signs) and the complex shape of some structures (e.g. arch bridges and roadway junctions). DSMs and LiDAR-based point clouds can be used during the post-processing phase to improve the geolocation accuracies of PSs and identify unwanted targets on the structure. High-resolution data can capture deformations for different parts of the structure and building information modelling (BIM) can be used to interpret measured deformations in relation to different structural components.
- To study the deformation of transport infrastructure, 1D LoS measurements obtained from MT-InSAR analysis need to be converted into 3D space, and possibly projected onto the structural reference system. However, due to the 1D nature of the sensor viewing geometry, deformations derived from a single acquisition geometry cannot fully capture the magnitude and direction of the actual displacement field. In addition, for the extreme case of movements occurring along a direction orthogonal to a satellite LoS, deformations cannot be measured. Consequently, without correct understanding or interpretation of LoS measurements, the actual deformation of a structure could be underestimated. While the simple projection of measurements from a single acquisition geometry could lead to large underestimations, the integration of MT-InSAR measurements with other monitoring data (e.g. GNSS) or the combined use of MT-InSAR data from multiple viewing geometries and sensors can help estimate 2D or 3D deformations more accurately.
- The magnitude of the maximum detectable deformation is limited by the cyclic nature of the phase and is thus connected to the sensor wavelength, while the detectable deformation rate is limited by the satellite revisit time. Consequently, large and/or fast structural deformations

may not be detected or may be incorrectly reconstructed in time/space, leading to unwrapping errors. Despite repeated efforts by the radar science community to resolve this technical limitation, the issue persists. More robust processing algorithms able to detect and resolve phase ambiguity are needed.
- The criteria used to assess the reliability of MT-InSAR measurements is another important limitation of the technology. There is the need for a quality estimator independent from the deformation model adopted during processing.
- Finally, to exploit the full potential of MT-InSAR for structural monitoring purposes, both the technology and products developed should be made more accessible to the civil engineering community. If the barrier to entry is lowered sufficiently, widespread industry adoption could ensue. To facilitate this, there needs to be more avenues to nurture cooperation between radar experts and the civil engineering community.

Acknowledgements

Valentina Macchiarulo was supported by a PhD scholarship granted by Sue and Roger Whorrod and the Alumni programme of the University of Bath. This publication is also part of project number OCENW.XS5.114 of the research programme Open Competition Domain Science – XS, which is financed by the Dutch Research Council (NWO).

REFERENCES

Achillopoulou DV, Mitoulis SA, Argyroudis SA and Wang Y (2020) Monitoring of transport infrastructure exposed to multiple hazards: a roadmap for building resilience. *Science of the Total Environment* **746**: 141001, https://doi.org/10.1016/j.scitotenv.2020.141001.

Alani AM, Tosti F, Bianchini Ciampoli L, Gagliardi V and Benedetto A (2020) An integrated investigative approach in health monitoring of masonry arch bridges using GPR and InSAR technologies. *NDT & E International* **115**: 102288, https://doi.org/10.1016/j.ndteint.2020.102288.

Alexakis H, Lau FDH and DeJong MJ (2021) Fibre optic sensing of ageing railway infrastructure enhanced with statistical shape analysis. *Journal of Civil Structural Health Monitoring* **11(1)**: 49–67, https://doi.org/10.1007/s13349-020-00437-w.

Ansari H, De Zan F and Parizzi A (2020) Study of systematic bias in measuring surface deformation with SAR interferometry. *IEEE Transactions on Geoscience and Remote Sensing* **59(2)**: 1285–1301, https://doi.org/10.1109/TGRS.2020.3003421.

Auer S, Hinz S and Bamler R (2009) Ray-tracing simulation techniques for understanding high-resolution SAR images. *IEEE Transactions on Geoscience and Remote Sensing* **48(3)**: 1445–1456, https://doi.org/10.1109/TGRS.2009.2029339.

Bakon M, Perissin D, Lazecky M and Papco J (2014) Infrastructure non-linear deformation monitoring via satellite radar interferometry. *Procedia Technology* **16**: 294–300, https://doi.org/10.1016/j.protcy.2014.10.095.

Balz T, Perissin D, Soergel U, Zhang L and Liao M (2009) Post-seismic infrastructure damage assessment using high-resolution SAR satellite data. *Proceedings of the 2nd International Conference on Earth Observation for Global Change, Chengdu, China* (Zhang X, Li J, Liu G and Yang X (eds)), vol. 7471, pp. 25–29.

Berardino P, Fornaro G, Lanari R and Sansosti E (2002) A new algorithm for surface deformation monitoring based on small baseline differential SAR interferograms. *IEEE Transactions on Geoscience and Remote Sensing* **40(11)**: 2375–2383, https://doi.org/10.1109/TGRS.2002.803792.

Bianchini S, Pratesi F, Nolesini T and Casagli N (2015) Building deformation assessment by means of persistent scatterer interferometry analysis on a landslide-affected area: the Volterra (Italy) case study. *Remote sensing* **7(4)**: 4678–4701, https://doi.org/10.3390/rs70404678.

Bonano M, Manunta M, Pepe A, Paglia L and Lanari R (2013) From previous C-band to new X-band SAR systems: assessment of the DInSAR mapping improvement for deformation time-series retrieval in urban areas. *IEEE Transactions on Geoscience and Remote Sensing* **51(4)**: 1973–1984, https://doi.org/10.1109/TGRS.2012.2232933.

Briggs K, Loveridge F and Glendinning S (2017) Failures in transport infrastructure embankments. *Engineering Geology* **219**: 107–117, https://doi.org/10.1016/j.enggeo.2016.07.016.

Bürgmann R, Hilley G, Ferretti A and Novali F (2006) Resolving vertical tectonics in the San Francisco Bay area from permanent scatterer InSAR and GPS analysis. *Geology* **34(3)**: 221–224, https://doi.org/10.1130/G22064.1.

Carnec C, Massonnet D and King C (1996) Two examples of the use of SAR interferometry on displacement fields of small spatial extent. *Geophysical Research Letters* **23(24)**: 3579–3582, https://doi.org/10.1029/96GL03042.

Casu F, Manconi A, Pepe A and Lanari R (2011) Deformation time-series generation in areas characterized by large displacement dynamics: the SAR amplitude pixel-offset SBAS technique. *IEEE Transactions on Geoscience and Remote Sensing* **49(7)**: 2752–2763, https://doi.org/10.1109/TGRS.2010.2104325.

Cavalagli N, Kita A, Falco S *et al.* (2019) Satellite radar interferometry and in situ measurements for static monitoring of historical monuments: the case of Gubbio, Italy. *Remote Sensing of Environment* **235**: 111453, https://doi.org/10.1016/j.rse.2019.111453.

Cerchiello V, Tessari G, Velterop E *et al.* (2017) Building damage risk by modeling interferometric time series. *IEEE Geoscience and Remote Sensing Letters* **14(4)**: 509–513, https://doi.org/10.1109/LGRS.2017.2651938.

Chang L and Hanssen RF (2014) Detection of cavity migration and sinkhole risk using radar interferometric time series. *Remote Sensing of Environment* **147**: 56–64, https://doi.org/10.1016/j.rse.2014.03.002.

Chang L and Hanssen R (2015a) A probabilistic approach for InSAR time-series postprocessing. *IEEE Transactions on Geoscience and Remote Sensing* **54(1)**: 421–430, https://doi.org/10.1109/TGRS.2015.2459037.

Chang L and Hanssen RF (2015b) Detection of permafrost sensitivity of the Qinghai–Tibet railway using satellite radar interferometry. *International Journal of Remote Sensing* **36(3)**: 691–700, https://doi.org/10.1080/01431161.2014.999886.

Chang L, Dollevoet RP and Hanssen RF (2016) Nationwide railway monitoring using satellite SAR interferometry. *IEEE Journal of Selected Topics in Applied Earth Observations and Remote Sensing* **10(2)**: 596–604, https://doi.org/10.1109/JSTARS.2016.2584783.

Chang L, Sakpal NP, Elberink SO and Wang H (2020) Railway infrastructure classification and instability identification using Sentinel-1 SAR and laser scanning data. *Sensors* **20(24)**: 7108, https://doi.org/10.3390/s20247108.

Chang PC, Flatau A and Liu S (2003) Health monitoring of civil infrastructure. *Structural Health Monitoring* **2(3)**: 257–267, https://doi.org/10.1177/1475921703036169.

Chen F, Lin H, Li Z, Chen Q and Zhou J (2012) Interaction between permafrost and infrastructure along the Qinghai–Tibet railway detected via jointly analysis of C-and L-band small baseline SAR interferometry. *Remote Sensing of Environment* **123**: 532–540, https://doi.org/10.1016/j.rse.2012.04.020.

Chen X, Achilli V, Fabris M *et al.* (2021) Combining sentinel-1 interferometry and ground-based geomatics techniques for monitoring buildings affected by mass movements. *Remote Sensing* **13(3)**: 452, https://doi.org/10.3390/rs13030452.

Cigna F, Lasaponara R, Masini N, Milillo P and Tapete D (2014a) Persistent scatterer interferometry processing of COSMO-SkyMed StripMap HIMAGE time series to depict deformation of the historic centre of Rome, Italy. *Remote Sensing* **6(12)**: 12593–12618, https://doi.org/10.3390/rs61212593.

Cigna F, Bateson LB, Jordan CJ and Dashwood C (2014b) Simulating SAR geometric distortions and predicting persistent scatterer densities for ERS-1/2 and ENVISAT C-band SAR and InSAR applications: Nationwide feasibility assessment to monitor the landmass of Great Britain with SAR imagery. *Remote Sensing of Environment* **152**: 441–466, https://doi.org/10.1016/j.rse.2014.06.025.

Colesanti C, Ferretti A, Novali F, Prati C and Rocca F (2003) SAR monitoring of progressive and seasonal ground deformation using the permanent scatterers technique. *IEEE Transactions on Geoscience and Remote Sensing* **41(7)**: 1685–1701, https://doi.org/10.1109/TGRS.2003.813278.

Colesanti C, Mouelic SL, Bennani M *et al.* (2005) Detection of mining related ground instabilities using the permanent scatterers technique – a case study in the east of France. *International Journal of Remote Sensing* **26(1)**: 201–207, https://doi.org/10.1080/0143116042000274069.

Costantini M, Malvarosa F, Minati F and Vecchioli F (2012) Multi-scale and block decomposition methods for finite difference integration and phase unwrapping of very large datasets in high resolution SAR interferometry. In *Proceedings of the 2012 IEEE International Geoscience and Remote Sensing Symposium*. IEEE, Piscataway, NJ, USA, pp. 5574–5577, https://doi.org/10.1109/IGARSS.2012.6352342.

Costantini M, Ferretti A, Minati F *et al.* (2017) Analysis of surface deformations over the whole Italian territory by interferometric processing of ERS, Envisat and COSMO-SkyMed radar data. *Remote Sensing of Environment* **202**: 250–275, https://doi.org/10.1016/j.rse.2017.07.017.

Crosetto M, Monserrat O, Cuevas-González M, Devanthéry N and Crippa B (2016) Persistent scatterer interferometry: a review. *ISPRS Journal of Photogrammetry and Remote Sensing* **115**: 78–89, https://doi.org/10.1016/j.isprsjprs.2015.10.011.

Crosetto M, Solari L, Mróz M *et al.* (2020) The evolution of wide-area DInSAR: from regional and national services to the European ground motion service. *Remote Sensing* **12(12)**: 2043, https://doi.org/10.3390/rs12122043.

Cuenca MC, Hanssen R, Hooper A and Arikan M (2011a) Surface deformation of the whole Netherlands after PSI analysis. In *Proceedings of Fringe 2011 Workshop, Frascati, Italy* (Ouwehand L (ed.)). ESA Special Publication, vol. 1, pp. 19–23.

Cuenca MC, Hooper AJ and Hanssen RF (2011b) A new method for temporal phase unwrapping of persistent scatterers InSAR time series. *IEEE Transactions on Geoscience and Remote Sensing* **49(11)**: 4606–4615, https://doi.org/10.1109/TGRS.2011.2143722.

Cusson D, Ghuman P, Gara M and McCardle A (2012) Remote monitoring of bridges from space. In *Proceedings of 54th Brazilian Conference on Concrete (CBC 2012)*, vol. 54, pp. 1–25.

Cusson D, Trischuk K, Hébert D *et al.* (2018) Satellite-based InSAR monitoring of highway bridges: validation case study on the north channel bridge in Ontario, Canada. *Transportation Research Record* **2672**: 76–86.

Cusson D, Rossi C and Ozkan IF (2020) Early warning system for the detection of unexpected bridge displacements from radar satellite data. *Journal of Civil Structural Health Monitoring* **11**: 189–204, https://doi.org/10.1007/s13349-020-00446-9.

Dalla Via G, Crosetto M and Crippa B (2012) Resolving vertical and east-west horizontal motion from differential interferometric synthetic aperture radar: the L'Aquila earthquake. *Journal of Geophysical Research: Solid Earth* **117(B2)**: B02310, https://doi.org/10.1029/2011JB008689.

De Luca C, Casu F, Manunta M, Onorato G and Lanari R (2021) Comments on 'Study of systematic bias in measuring surface deformation with SAR interferometry'. *IEEE Transactions on Geoscience and Remote Sensing*, https://doi.org/10.1109/TGRS.2021.3103037.

Del Soldato M, Tomás R, Pont Castillo J *et al.* (2016) A multi-sensor approach for monitoring a road bridge in the Valencia harbor (SE Spain) by SAR interferometry (InSAR). *Rendiconti Online della Società Gelogica Italiana* **41**: 235–238, https://doi.org/10.3301/ROL.2016.137.

Delgado Blasco J, Foumelis M, Stewart C and Hooper A (2019) Measuring urban subsidence in the Rome metropolitan area (Italy) with sentinel-1 SNAP-StaMPS persistent scatterer interferometry. *Remote Sensing* **11(2)**: 129, https://doi.org/10.3390/rs11020129.

DePrekel K, Bouali E and Oommen T (2018) Monitoring the impact of groundwater pumping on infrastructure using geographic information system (GIS) and persistent scatterer interferometry (PSI). *Infrastructures* **3(4)**: 57, https://doi.org/10.3390/infrastructures3040057.

Di Martire D, Iglesias R, Monells D *et al.* (2014) Comparison between differential SAR interferometry and ground measurements data in the displacement monitoring of the earth-dam of Conza della Campania (Italy). *Remote Sensing of Environment* **148**: 58–69, https://doi.org/10.1016/j.rse.2014.03.014.

Drougkas A, Verstrynge E, Van Balen K *et al.* (2020) Country-scale InSAR monitoring for settlement and uplift damage calculation in architectural heritage structures. *Structural Health Monitoring*, https://doi.org/10.1177/1475921720942120.

ESA (European Space Agency) (2021) *eoPortal Directory - Satellite Missions Database*. ESA, Paris, France. See https://directory.eoportal.org/web/eoportal/satellite-missions/ (accessed 13/12/2021).

Ferretti A, Prati C and Rocca F (2000) Nonlinear subsidence rate estimation using permanent scatterers in differential SAR interferometry. *IEEE Transactions on Geoscience and Remote Sensing* **38(5)**: 2202–2212, https://doi.org/10.1109/36.868878.

Ferretti A, Prati C and Rocca F (2001) Permanent scatterers in SAR interferometry. *IEEE Transactions on Geoscience and Remote Sensing* **39(1)**: 8–20, https://doi.org/10.1109/36.898661.

Ferretti A, Savio G, Barzaghi R *et al.* (2007) Submillimeter accuracy of InSAR time series: experimental validation. *IEEE Transactions on Geoscience and Remote Sensing* **45(5)**: 1142–1153, https://doi.org/10.1109/TGRS.2007.894440.

Flores-Anderson AI, Herndon KE, Thapa RB and Cherrington E (2019) *The SAR Handbook: Comprehensive Methodologies for Forest Monitoring and Biomass Estimation*. SERVIR Global Science. National Space Science and Technology Center, Washington, DC, USA.

Fornaro G, Reale D and Verde S (2013) Bridge thermal dilation monitoring with millimeter sensitivity via multidimensional SAR imaging. *IEEE Geoscience and Remote Sensing Letters* **10(4)**: 677–681, https://doi.org/10.1109/LGRS.2012.2218214.

Franceschetti G, Iodice A and Riccio D (2002) A canonical problem in electromagnetic backscattering from buildings. *IEEE Transactions on Geoscience and Remote Sensing* **40(8)**: 1787–1801, https://doi.org/10.1109/TGRS.2002.802459.

Fuhrmann T and Garthwaite MC (2019) Resolving three-dimensional surface motion with InSAR: constraints from multi-geometry data fusion. *Remote Sensing* **11(3)**: 241, https://doi.org/10.3390/rs11030241.

Fuhrmann T, Caro Cuenca M, Knöpfler A *et al.* (2015) Estimation of small surface displacements in the upper Rhine Graben area from a combined analysis of PS-InSAR, levelling and GNSS data. *Geophysical Journal International* **203(1)**: 614–631, https://doi.org/10.1093/gji/ggv328.

Gabriel A, Goldstein R and Zebker H (1989) Mapping small elevation changes over large areas: differential radar interferometry. *Journal of Geophysical Research: Solid Earth* **94(B7)**: 9183–9191.

García-Davalillo JC, Herrera G, Notti D, Strozzi T and Álvarez-Fernández I (2014) DInSAR analysis of ALOS PALSAR images for the assessment of very slow landslides: the Tena valley case study. *Landslides* **11(2)**: 225–246, https://doi.org/10.1007/s10346-012-0379-8.

Ge D, Wang Y, Zhang L *et al.* (2009) Using permanent scatterer InSAR to monitor land subsidence along high speed railway-the first experiment in China. In *Proceedings of the Workshop Fringe 2009 – Advances in the Science and Applications of SAR Interferometry* (Lacoste H (ed.)). ESA-SP, Noordwijk, the Netherlands, vol. 677, p. 30.

Gebert N, Krieger G and Moreira A (2006) Digital beamforming for HRWS-SAR imaging: system design, performance and optimization strategies. In *Proceedings of the 2006 IEEE International Symposium on Geoscience and Remote Sensing*. IEEE, Piscataway, NJ, USA, pp. 1836–1839, https://doi.org/10.1109/IGARSS.2006.474.

Gernhardt S, Adam N, Eineder M and Bamler R (2010) Potential of very high resolution SAR for persistent scatterer interferometry in urban areas. *Annals of GIS* **16(2)**: 103–111, https://doi.org/10.1080/19475683.2010.492126.

Gernhardt S, Cong X, Eineder M, Hinz S and Bamler R (2011) Geometrical fusion of multitrack PS point clouds. *IEEE Geoscience and Remote Sensing Letters* **9(1)**: 38–42, https://doi.org/10.1109/LGRS.2011.2159190.

Giardina G, Milillo P, DeJong MJ, Perissin D and Milillo G (2019) Evaluation of InSAR monitoring data for post-tunnelling settlement damage assessment. *Structural Control and Health Monitoring* **26(2)**: e2285, https://doi.org/10.1002/stc.2285.

Goldstein RM, Engelhardt H, Kamb B and Frolich RM (1993) Satellite radar interferometry for monitoring ice sheet motion: application to an Antarctic ice stream. *Science* **262(5139)**: 1525–1530.

Gomba G, Parizzi A, De Zan F, Eineder M and Bamler R (2015) Toward operational compensation of ionospheric effects in SAR interferograms: the split-spectrum method. *IEEE Transactions on Geoscience and Remote Sensing* **54(3)**: 1446–1461, https://doi.org/10.1109/TGRS.2015.2481079.

Hadjidemetriou GM, Herrera M and Parlikad AK (2021) Condition and criticality-based predictive maintenance prioritisation for networks of bridges. *Structure and Infrastructure Engineering* 1–16, https://doi.org/10.1080/15732479.2021.1897146.

Hanssen RF (2001) *Radar Interferometry: Data Interpretation and Error Analysis*. Springer Science + Business Media, Dordrecht, the Netherlands.

Hanssen RF (2005) Satellite radar interferometry for deformation monitoring: a priori assessment of feasibility and accuracy. *International Journal of Applied Earth Observation and Geoinformation* **6(3–4)**: 253–260, https://doi.org/10.1016/j.jag.2004.10.004.

Hooper A and Zebker HA (2007) Phase unwrapping in three dimensions with application to InSAR time series. *Journal of the Optical Society of America A* **24(9)**: 2737–2747, https://doi.org/10.1364/JOSAA.24.002737.

Hoppe E, Bruckno B, Campbell E *et al.* (2016) Transportation infrastructure monitoring using satellite remote sensing. *Materials and Infrastructures* **15**: 185–198, https://doi.org/10.1002/9781119318583.ch14.

Hoppe EJ, Novali F, Rucci A *et al.* (2019) Deformation monitoring of posttensioned bridges using high-resolution satellite remote sensing. *Journal of Bridge Engineering* **24(12)**: 04019115, https://doi.org/10.1061/(ASCE)BE.1943-5592.0001479.

Hu J, Li Z, Ding X *et al.* (2014) Resolving three-dimensional surface displacements from InSAR measurements: a review. *Earth-Science Reviews* **133**: 1–17, https://doi.org/10.1016/j.earscirev.2014.02.005.

Huang Q, Monserrat O, Crosetto M *et al.* (2018) Displacement monitoring and health evaluation of two bridges using sentinel-1 SAR images. *Remote Sensing* **10(11)**: 1714, https://doi.org/10.3390/rs10111714.

Ignatenko V, Laurila P, Radius A *et al.* (2021) ICEYE microsatellite SAR constellation status update: evaluation of first commercial imaging modes. In *Proceedings of IGARSS 2020 IEEE International Geoscience and Remote Sensing Symposium*. IEEE, Piscataway, NJ, USA, pp. 3581–3584, https://doi.org/10.1109/IGARSS39084.2020.9324531.

Infante D, Di Martire D, Calcaterra D *et al.* (2019) Integrated procedure for monitoring and assessment of linear infrastructures safety (I-Pro MONALISA) affected by slope instability. *Applied Sciences* **9(24)**: 5535, https://doi.org/10.3390/app9245535.

Jolivet R, Grandin R, Lasserre C, Doin MP and Peltzer G (2011) Systematic InSAR tropospheric phase delay corrections from global meteorological reanalysis data. *Geophysical Research Letters* **38(17)**: 1–6, https://doi.org/10.1029/2011GL048757.

Jung J, Kim DJ, Palanisamy Vadivel SK and Yun SH (2019) Long-term deflection monitoring for bridges using X and C-band time-series SAR interferometry. *Remote Sensing* **11(11)**: 1258, https://doi.org/10.3390/rs11111258.

Kampes MKB (2006) *Radar Interferometry: Persistent Scatterers Technique*. Springer, Dordrecht, the Netherlands.

Lanari R, Mora O, Manunta M *et al.* (2004) A small-baseline approach for investigating deformations on full-resolution differential SAR interferograms. *IEEE Transactions on Geoscience and Remote Sensing* **42(7)**: 1377–1386, https://doi.org/10.1109/TGRS.2004.828196.

Lazecky M, Hlavacova I, Bakon M *et al.* (2016) Bridge displacements monitoring using space-borne X-band SAR interferometry. *IEEE Journal of Selected Topics in Applied Earth Observations and Remote Sensing* **10(1)**: 205–210, https://doi.org/10.1109/JSTARS.2016.2587778.

Luo H, Li Z, Dong Z *et al.* (2019) A new baseline linear combination algorithm for generating urban digital elevation models with multitemporal InSAR observations. *IEEE Transactions on Geoscience and Remote Sensing* **58(2)**: 1120–1133, https://doi.org/10.1109/TGRS.2019.2943919.

Ma P, Li T, Fang C and Lin H (2019) A tentative test for measuring the sub-millimeter settlement and uplift of a high-speed railway bridge using COSMO-SkyMed images. *ISPRS Journal of*

Photogrammetry and Remote Sensing **155**: 1–12, https://doi.org/10.1016/j.isprsjprs.2019.06.013.

Macchiarulo V, Milillo P, Blenkinsopp C and Giardina G (2021a) Monitoring deformations of infrastructure networks: a fully automated GIS integration and analysis of InSAR time-series. *Structural Health Monitoring*, 1045912 (in press).

Macchiarulo V, Milillo P, DeJong MJ *et al.* (2021b) Integrated InSAR monitoring and structural assessment of tunnelling-induced building deformations. *Structural Control and Health Monitoring* **28(9)**: e2781, https://doi.org/10.1002/stc.2781.

Massonnet D and Feigl K (1998) Radar interferometry and its application to changes in the Earth's surface. *Reviews of Geophysics* **36(4)**: 441–500, https://doi.org/10.1029/97RG03139.

Meyer FJ, Ajadi OA and Hoppe EJ (2020) Studying the applicability of X-band SAR data to the network-scale mapping of pavement roughness on US roads. *Remote Sensing* **12(9)**: 1507, https://doi.org/10.3390/rs12091507.

Milillo P, Riel B, Minchew B *et al.* (2015) On the synergistic use of SAR constellations' data exploitation for earth science and natural hazard response. *IEEE Journal of Selected Topics in Applied Earth Observations and Remote Sensing* **9(3)**: 1095–1100, https://doi.org/10.1109/JSTARS.2015.2465166.

Milillo P, Bürgmann R, Lundgren P *et al.* (2016a) Space geodetic monitoring of engineered structures: the ongoing destabilization of the Mosul dam, Iraq. *Scientific Reports* **6**: 37408, https://doi.org/10.1038/srep37408.

Milillo P, Perissin D, Salzer JT *et al.* (2016b) Monitoring dam structural health from space: insights from novel InSAR techniques and multi-parametric modeling applied to the Pertusillo dam Basilicata, Italy. *International Journal of Applied Earth Observation and Geoinformation* **52**: 221–229, https://doi.org/10.1016/j.jag.2016.06.013.

Milillo P, Giardina G, DeJong MJ, Perissin D and Milillo G (2018) Multi-temporal InSAR structural damage assessment: the London Crossrail case study. *Remote Sensing* **10(2)**: 287, https://doi.org/10.3390/rs10020287.

Milillo P, Rignot E, Rizzoli P *et al.* (2019a) Heterogeneous retreat and ice melt of Thwaites glacier, West Antarctica. *Science Advances* **5(1)**: eaau3433, https://doi.org/10.1126/sciadv.aau3433.

Milillo P, Giardina G, Perissin D *et al.* (2019b) Pre-collapse space geodetic observations of critical infrastructure: the Morandi Bridge, Genoa, Italy. *Remote Sensing* **11(12)**: 1403, https://doi.org/10.3390/rs11121403.

Milillo P, Giardina G, Perissin D (2020) Reply to Lanari, R. *et al.* Comment on 'Pre-collapse space geodetic observations of critical infrastructure: the Morandi bridge, Genoa, Italy' by Milillo *et al.* (2019). *Remote Sensing* **12(24)**: 4016, https://doi.org/10.3390/rs12244016.

Monserrat O, Crosetto M, Cuevas M and Crippa B (2011) The thermal expansion component of persistent scatterer interferometry observations. *IEEE Geoscience and Remote Sensing Letters* **8(5)**: 864–868, https://doi.org/10.1109/LGRS.2011.2119463.

Montazeri S, Rodríguez González F and Zhu XX (2018) Geocoding error correction for InSAR point clouds. *Remote Sensing* **10(10)**: 1523, https://doi.org/10.3390/rs10101523.

Moreira A, Prats-Iraola P, Younis M *et al.* (2013) A tutorial on synthetic aperture radar. *IEEE Geoscience and Remote Sensing Magazine* **1(1)**: 6–43, https://doi.org/10.1109/MGRS.2013.2248301.

Nahli A, Simonetto E, Tatin M *et al.* (2020) On the combination of PSInSAR and GNSS techniques for long-term bridge monitoring. *The International Archives of Photogrammetry, Remote Sensing and Spatial Information Sciences* **43**: 325–332, https://doi.org/10.5194/isprs-archives-XLIII-B3-2020-325-2020.

Osmanoğlu B, Dixon TH, Wdowinski S, Cabral-Cano E and Jiang Y (2011) Mexico City subsidence observed with persistent scatterer InSAR. *International Journal of Applied Earth Observation and Geoinformation* **13(1)**: 1–12, https://doi.org/10.1016/j.jag.2010.05.009.

Peduto D, Cascini L, Arena L *et al.* (2015) A general framework and related procedures for multiscale analyses of DInSAR data in subsiding urban areas. *ISPRS Journal of Photogrammetry and Remote Sensing* **105**: 186–210, https://doi.org/10.1016/j.isprsjprs.2015.04.001.

Peduto D, Nicodemo G, Maccabiani J and Ferlisi S (2017) Multi-scale analysis of settlement-induced building damage using damage surveys and DInSAR data: a case study in the Netherlands. *Engineering Geology* **218**: 117–133, https://doi.org/10.1016/j.enggeo.2016.12.018.

Perissin D (2008) Validation of the submetric accuracy of vertical positioning of PSs in C-band. *IEEE Geoscience and Remote Sensing Letters* **5(3)**: 502–506, https://doi.org/10.1109/LGRS.2008.921210.

Perissin D and Ferretti A (2007) Urban-target recognition by means of repeated spaceborne SAR images. *IEEE Transactions on Geoscience and Remote Sensing* **45(12)**: 4043–4058, https://doi.org/10.1109/TGRS.2007.906092.

Perissin D and Rocca F (2006) High-accuracy urban DEM using permanent scatterers. *IEEE Transactions on Geoscience and Remote Sensing* **44(11)**: 3338–3347, https://doi.org/10.1109/TGRS.2006.877754.

Perissin D and Wang T (2011) Repeat-pass SAR interferometry with partially coherent targets. *IEEE Transactions on Geoscience and Remote Sensing* **50(1)**: 271–280, https://doi.org/10.1109/TGRS.2011.2160644.

Perissin D, Wang Z and Wang T (2011) The SARPROZ InSAR tool for urban subsidence/manmade structure stability monitoring in China. In *Proceedings of the ISRSE, Sydney, Australia*, vol. 1015.

Perissin D, Wang Z and Lin H (2012) Shanghai subway tunnels and highways monitoring through Cosmo-SkyMed persistent scatterers. *ISPRS Journal of Photogrammetry and Remote Sensing* **73**: 58–67, https://doi.org/10.1016/j.isprsjprs.2012.07.002.

Prats-Iraola P, Scheiber R, Rodríguez-Cassolà M *et al.* (2012) High precision SAR focusing of TerraSAR-X experimental staring spotlight data. In *Proceedings of the 2012 IEEE International Geoscience and Remote Sensing Symposium*. IEEE, Piscataway, NJ, USA, pp. 3576–3579, https://doi.org/10.1109/IGARSS.2012.6350644.

Pregnolato M (2019) Bridge safety is not for granted – a novel approach to bridge management. *Engineering Structures* **196**: 109193, https://doi.org/10.1016/j.engstruct.2019.05.035.

Qin X, Zhang L, Yang M *et al.* (2018) Mapping surface deformation and thermal dilation of arch bridges by structure-driven multi-temporal DInSAR analysis. *Remote Sensing of Environment* **216**: 71–90, https://doi.org/10.1016/j.rse.2018.06.032.

Raspini F, Bianchini S, Ciampalini A *et al.* (2018) Continuous, semi-automatic monitoring of ground deformation using Sentinel-1 satellites. *Scientific Reports* **8(1)**: 1–11, https://doi.org/10.1038/s41598-018-25369-w.

Reale D, Noviello C, Verde S *et al.* (2019) A multi-disciplinary approach for the damage analysis of cultural heritage: the case study of the St. Gerlando Cathedral in Agrigento. *Remote Sensing of Environment* **235**: 111464, https://doi.org/10.1016/j.rse.2019.111464.

Refice A, Pasquariello G and Bovenga F (2020) Model-free characterization of SAR MTI time series. *IEEE Geoscience and*

Remote Sensing Letters **19**: 4004405, https://doi.org/10.1109/LGRS.2020.3031655.

Reigber A and Ferro-Famil L (2005) Interference suppression in synthesized SAR images. *IEEE Geoscience and Remote Sensing Letters* **2(1)**: 45–49, https://doi.org/10.1109/LGRS.2004.838419.

Rosen PA, Hensley S, Joughin I *et al.* (2000) Synthetic aperture radar interferometry. *Proceedings of the IEEE* 88(3): 333–382, https://doi.org/10.1109/5.838084.

Rosen PA, Horst SJ, Khazendar A *et al.* (2019) NASA's next generation surface deformation and change observing system architecture. In *Proceedings of IGARSS 2019 IEEE International Geoscience and Remote Sensing Symposium*. IEEE, Piscataway, NJ, USA, pp. 8378–8380, https://doi.org/10.1109/IGARSS.2019.8899231.

Rucci A, Ferretti A, Guarnieri AM and Rocca F (2012) Sentinel 1 SAR interferometry applications: the outlook for sub millimeter measurements. *Remote Sensing of Environment* **120**: 156–163, https://doi.org/10.1016/j.rse.2011.09.030.

Salzer J, Milillo P, Varley N *et al.* (2017) Evaluating links between deformation, topography and surface temperature at volcanic domes: results from a multi-sensor study at Volcán de Colima, Mexico. *Earth and Planetary Science Letters* **479**: 354–365, https://doi.org/10.1016/j.epsl.2017.09.027.

Selvakumaran S, Plank S, Geiß C, Rossi C and Middleton C (2018) Remote monitoring to predict bridge scour failure using interferometric synthetic aperture radar (InSAR) stacking techniques. *International Journal of Applied Earth Observation and Geoinformation* **73**: 463–470, https://doi.org/10.1016/j.jag.2018.07.004.

Selvakumaran S, Rossi C, Marinoni A *et al.* (2020) Combined InSAR and terrestrial structural monitoring of bridges. *IEEE Transactions on Geoscience and Remote Sensing* **216(10)**: 71–90, https://doi.org/10.1109/TGRS.2020.2979961.

Selvakumaran S, Rossi C, Barton E and Middleton C (2021) Interferometric synthetic aperture radar (InSAR) in the context of bridge monitoring. In *Advances in Remote Sensing for Infrastructure Monitoring* (Singhroy V (ed.)). Springer Nature, Cham, Switzerland, pp. 183–209, https://doi.org/10.1007/978-3-030-59109-08.

Shimoni M, Lopez J, Walstra J *et al.* (2017) GEPATAR: a geotechnical based PS-InSAR toolbox for architectural conservation in Belgium. In *Proceedings of the 2017 IEEE International Geoscience and Remote Sensing Symposium*. IEEE, Piscataway, NJ, USA, pp. 5555–5558, https://doi.org/10.1109/IGARSS.2017.8128263.

Solano-Rojas D, Wdowinski S, Cabral-Cano E and Osmanoğlu B (2020) Detecting differential ground displacements of civil structures in fast-subsiding metropolises with interferometric SAR and band-pass filtering. *Scientific Reports* **10(1)**: 1–14, https://doi.org/10.1038/s41598-020-72293-z.

Solari L, Ciampalini A, Raspini F, Bianchini S and Moretti S (2016) PSInSAR analysis in the Pisa urban area (Italy): a case study of subsidence related to stratigraphical factors and urbanization. *Remote Sensing* **8(2)**: 120, https://doi.org/10.3390/rs8020120.

Sousa JJ and Bastos L (2013) Multi-temporal SAR interferometry reveals acceleration of bridge sinking before collapse. *Natural Hazards and Earth System Sciences* **13(3)**: 659–667, https://doi.org/10.5194/nhess-13-659-2013.

Sousa JJ, Hooper AJ, Hanssen RF, Bastos LC and Ruiz AM (2011) Persistent scatterer InSAR: a comparison of methodologies based on a model of temporal deformation vs. spatial correlation selection criteria. *Remote Sensing of Environment* **115(10)**: 2652–2663, https://doi.org/10.1016/j.rse.2011.05.021.

Stramondo S, Bozzano F, Marra F *et al.* (2008) Subsidence induced by urbanisation in the city of Rome detected by advanced InSAR technique and geotechnical investigations. *Remote Sensing of Environment* **112(6)**: 3160–3172, https://doi.org/10.1016/j.rse.2008.03.008.

Stringham C, Farquharson G, Castelletti D *et al.* (2019) The Capella X-band SAR constellation for rapid imaging. In *Proceedings of IGARSS 2019 IEEE International Geoscience and Remote Sensing Symposium*. IEEE, Piscataway, NJ, USA, pp. 9248–9251, https://doi.org/10.1109/IGARSS.2019.8900410.

Teatini P, Tosi L, Strozzi T *et al.* (2005) Mapping regional land displacements in the Venice coastland by an integrated monitoring system. *Remote Sensing of Environment* **98(4)**: 403–413, https://doi.org/10.1016/j.rse.2005.08.002.

Usai S (2003) A least squares database approach for SAR interferometric data. *IEEE Transactions on Geoscience and Remote Sensing* **41(4)**: 753–760, https://doi.org/10.1109/TGRS.2003.810675.

van Breugel K (2017) Ageing infrastructure and circular economy: challenges and risks. In *Proceedings of the 2nd World Congress on Civil, Structural, and Environmental Engineering (CSEE'17), Barcelona, Spain*. Avestia Publishing, Orleans, ON, Canada. https://doi.org/10.11159/icesdp17.1.

van Leijen FJ (2014) *Persistent Scatterer Interferometry Based on Geodetic Estimation Theory*. Doctoral thesis, TU Delft, Delft, the Netherlands, https://doi.org/10.4233/uuid:5dba48d7-ee26-4449-b674-caa8df93e71e.

Worden K and Dulieu-Barton JM (2004) An overview of intelligent fault detection in systems and structures. *Structural Health Monitoring* **3(1)**: 85–98, https://doi.org/10.1177/1475921704041866.

Wright TJ, Parsons BE and Lu Z (2004) Toward mapping surface deformation in three dimensions using InSAR. *Geophysical Research Letters* **31(1)**: L01607, https://doi.org/10.1029/2003GL018827.

Wu S, Zhang L, Ding X and Perissin D (2018) Pixel-wise MTInSAR estimator for integration of coherent point selection and unwrapped phase vector recovery. *IEEE Transactions on Geoscience and Remote Sensing* **57(5)**: 2659–2668, https://doi.org/10.1109/TGRS.2018.2876115.

Xie C, Li Z, Xu J and Li X (2010) Analysis of deformation over permafrost regions of Qinghai–Tibet plateau based on permanent scatterers. *International Journal of Remote Sensing* **31(8)**: 1995–2008, https://doi.org/10.1080/01431160902929255.

Yan Y, Doin MP, Lopez-Quiroz P *et al.* (2012) Mexico city subsidence measured by InSAR time series: joint analysis using PS and SBAS approaches. *IEEE Journal of Selected Topics in Applied Earth Observations and Remote Sensing* **5(4)**: 1312–1326, https://doi.org/10.1109/JSTARS.2012.2191146.

Yang M, Dheenathayalan P, Chang L *et al.* (2016) High-precision 3D geolocation of persistent scatterers with one single-Epoch GCP and LIDAR DSM data. In *Proceedings of European Space Agency Living Planet Symposium 2016* (Ouwehand L (ed.)). European Space Agency, Noordwijk, the Netherlands, p. 398.

Yun SH, Hudnut K, Owen S *et al.* (2015) Rapid damage mapping for the 2015 M w 7.8 Gorkha earthquake using synthetic aperture radar data from COSMO–SkyMed and ALOS-2 satellites. *Seismological Research Letters* **86(6)**: 1549–1556, https://doi.org/10.1785/0220150152.

Zebker HA and Rosen PA (2020) The case for 6-hour repeat InSAR. In *Proceedings of IGARSS 2020 IEEE International Geoscience and Remote Sensing Symposium*. IEEE, Piscataway, NJ, USA, pp. 5949–5952, https://doi.org/10.1109/IGARSS39084.2020.9323894.

Zhao J, Wu J, Ding X and Wang M (2017) Elevation extraction and deformation monitoring by multitemporal InSAR of Lupu Bridge in Shanghai. *Remote Sensing* **9(9)**: 897, https://doi.org/10.3390/rs9090897.

Zhou F, Wu R, Xing M and Bao Z (2007) Eigensubspace-based filtering with application in narrow-band interference suppression for SAR. *IEEE Geoscience and Remote Sensing Letters* **4(1)**: 75–79, https://doi.org/10.1109/LGRS.2006.887033.

Zhu M, Wan X, Fei B *et al.* (2018) Detection of building and infrastructure instabilities by automatic spatiotemporal analysis of satellite SAR interferometry measurements. *Remote Sensing* **10(11)**: 1816, https://doi.org/10.3390/rs10111816.